Signatures of reductive magnetic mineral diagenesis from unmixing of first-order reversal curves

Andrew P. Roberts[1], Xiang Zhao[1], Richard J. Harrison[2], David Heslop[1], Adrian R. Muxworthy[3], Christopher J. Rowan[4], Juan-Cruz Larrasoaña[5], and Fabio Florindo[6]

1. Research School of Earth Sciences, Australian National University, Canberra, ACT 2601, Australia
2. Department of Earth Sciences, University of Cambridge, Cambridge, CB2 3EQ, UK
3. Department of Earth Science and Engineering, Imperial College London, South Kensington Campus, London, SW7 2AZ, UK
4. Department of Geology, Kent State University, 325 Lincoln Street, Kent, OH 44240, USA
5. Instituto Geológico y Minero de España, Unidad de Zaragoza, C/ Manuel Lasala 44, 9B, Zaragoza 50006, Spain
6. Institute of Earth Sciences Jaume Almera, Consejo Superior de Investigaciones Científicas, Barcelona 08028, Spain
7. Istituto Nazionale di Geofisica e Vulcanologia, Via di Vigna Murata 605, 00143 Rome, Italy

Abstract

Diagenetic alteration of magnetic minerals occurs in all sedimentary environments and tends to be severe in reducing environments. Magnetic minerals provide useful information about sedimentary diagenetic processes, which makes it valuable to use magnetic properties to identify the diagenetic environment in which the magnetic minerals occur and to inform interpretations of paleomagnetic recording or environmental processes. We use a newly developed first-order reversal curve (FORC) unmixing method on well-studied samples to illustrate how magnetic

properties can be used to assess diagenetic processes in reducing sedimentary environments. From our analysis of multiple data sets, consistent magnetic components are identified for each stage of reductive diagenesis. Relatively unaltered detrital and biogenic magnetic mineral assemblages in surficial oxic to manganous diagenetic environments undergo progressive dissolution with burial into ferruginous and sulfidic environments, and largely disappear at the sulfate-methane transition (SMT). Below the SMT, a weak superparamagnetic to largely non-interacting stable single domain (SD) greigite component is observed in all studied data sets. Moderately interacting stable SD authigenic pyrrhotite and strongly interacting stable SD greigite are observed commonly in methanic environments. Recognition of these characteristic magnetic components enables identification of key diagenetic processes and should help to constrain interpretation of magnetic mineral assemblages in future studies. A key question for future studies concerns whether stable SD greigite forms in the sulfidic or methanic zones, where formation in deeper methanic sediments will cause greater delays in paleomagnetic signal recording. Authigenic pyrrhotite forms in methanic environments, so it will usually record a delayed paleomagnetic signal.

1. Introduction

Magnetic mineral diagenesis involves the post-depositional modification of magnetic particles either by alteration of detrital sedimentary minerals or by authigenic growth of secondary magnetic minerals (Roberts, 2015). Diagenesis affects all sedimentary magnetic mineral assemblages, which makes it important to assess the extent of its effects. Diagenetic effects range from subtle (e.g., minor surficial oxidation of detrital/biogenic magnetic particles) to pervasive (e.g., complete dissolution of detrital/biogenic particles or growth of new authigenic phases that dominate the magnetic signal). Diagenetic magnetic mineral modification occurs over the full range of oxidizing to reducing conditions (Figure 1). Under oxic conditions, Fe^{2+} within magnetic minerals is oxidized progressively to Fe^{3+}. Under reducing conditions, Fe^{3+} within magnetic

minerals is reduced to Fe^{2+}, which is achieved by corrosion of detrital/biogenic magnetic minerals, and incorporation of the liberated Fe^{2+} into authigenic pyrite or other paramagnetic phases. Reductive diagenesis is driven by microbial degradation of organic matter where different oxidants are used progressively with the following order of electron acceptor use: oxygen, nitrate, manganese oxides, iron (oxyhydr-)oxides, sulfate, and organic matter itself (Figure 1). When one oxidant is depleted, the next most efficient (i.e., most energy producing) oxidant is used, etc., until either all oxidants or all reactive organic matter are consumed (Froelich et al., 1979). In some settings, two respiration processes can occur simultaneously (e.g., Oremland and Taylor, 1978; Canfield and Thamdrup, 2009). The treatment provided here is based on the normal progression of environments expected during steady-state diagenesis (Figure 1).

Magnetic minerals start to dissolve in ferruginous environments in association with iron reduction, and dissolution becomes pervasive in sulfidic environments where pore water sulfate is consumed entirely via microbial sulfate reduction or by anaerobic oxidation of methane (AOM) in underlying methanic environments, where the dominant process by which organic matter is degraded is via methanogenesis (Canfield and Thamdrup, 2009; Roberts, 2015). The ferruginous, sulfidic, and methanic diagenetic zones represent the more strongly reducing end of the spectrum in which the effects of diagenesis on magnetic mineral assemblages become pervasive. These environments are encountered frequently in paleomagnetic and environmental magnetic studies, which makes it important to have a thorough understanding of the types of magnetic mineral assemblages that occur in these settings and the diagenetic processes that modify or control them.

A key aim in rock magnetism over the last 20 years has been to develop techniques that enable identification of individual magnetic mineral components. This is important in most paleomagnetic and environmental magnetic applications where magnetic signals are carried by mixed magnetic mineral assemblages. For example, even in seemingly simple pelagic carbonate sediments, four or five distinct magnetic mineral components are identified commonly (Roberts et

al., 2013). Each component can potentially carry valuable environmental information; being able to unmix rigorously the magnetic signals carried by such materials can unlock this environmental information. Magnetic unmixing is also valuable in paleomagnetic studies, where, for example, sedimentary relative paleointensity signals are recorded with different efficiency by co-occurring detrital and biogenic magnetite (Ouyang et al., 2014; Chen et al., 2017). Various unmixing methods have been developed, which generally involve fitting of functions to derivatives of isothermal remanent magnetization (IRM) acquisition or direct current demagnetization curves (e.g., Robertson & France, 1994; Kruiver et al., 2001; Heslop et al., 2002; Heslop & Dillon, 2007) or to alternating field demagnetization curves of an anhysteretic remanent magnetization or IRM (Egli, 2004a, b, c). A key issue with magnetic unmixing is that, like any geophysical inversion method, potentially infinite combinations of components can be fitted to a given coercivity spectrum unless independent evidence is available concerning magnetic components (Heslop, 2015). So-called semi-supervised or supervised unmixing is, therefore, needed to minimize ambiguities associated with spectral unmixing approaches (Heslop, 2015).

First-order reversal curve (FORC) diagrams (Pike et al., 1999; Roberts et al., 2000) are used widely in rock magnetism because of their diagnostic value in identifying magnetic domain states and magnetostatic interactions for magnetic mineral components (Roberts et al., 2014). FORC measurements provide information about the magnetic response of all particles in a sample in terms of magnetization (represented by the magnitude of the FORC distribution), and the coercivity and magnetic interaction field distributions (B_c and B_i axes of the FORC diagram, respectively), where contrasting features can be used to diagnose the full range of magnetic domain states in fine magnetic particle systems. FORC distributions are, therefore, powerful for exploring subtle magnetization processes that are unrecognizable in standard hysteresis measurements. For readers who are less familiar with FORC diagrams, we show typical FORC diagrams in Figure 2 and refer here to papers that describe the key features for the following types

of particle systems: superparamagnetic (SP; Pike et al., 2001a), stable single domain (SD) with and without interactions (Pike et al., 1999; Roberts et al., 2000, 2014), vortex (Pike & Fernandez, 1999; Roberts et al., 2000, 2017; Muxworthy & Dunlop, 2002), and multi-domain (MD; Pike et al., 2001b). Despite their widespread use, most applications of FORC diagrams have only involved qualitative domain state identification or quantitative assessment of interactions (e.g., Muxworthy & Dunlop, 2002; Carvallo et al., 2006) without quantifying the contributions from each magnetic mineral component present in a sample, although some more quantitative attempts have had limited success (Muxworthy et al., 2005). This situation has changed with development of tools that enable quantitative simulation of FORC distributions (Harrison & Lascu, 2014) and with introduction of principal component analysis (PCA) to unmix FORC distributions (Heslop et al., 2014) into end-member (EM) components (Lascu et al., 2015). An important aspect of unmixing is to solve the linear mixing equation (Heslop, 2015), which was not achieved in the FORC-PCA approach of Lascu et al. (2015). Harrison et al. (2018), therefore, further developed FORC unmixing to solve this equation.

In this paper, we use the new FORC unmixing algorithm of Harrison et al. (2018), which is built into the FORCinel software package (Harrison & Feinberg, 2008), to illustrate its power for understanding magnetic particle assemblages in sedimentary sequences that have undergone reductive diagenesis. Our aim is to reveal diagenetic processes through identification of the magnetic minerals present in these diagenetic systems. The identified magnetic components should be useful for future studies of similar diagenetic environments in which these components are expected to be encountered, where FORC unmixing can enable quantitative assessment of their respective contributions. Typical FORC diagrams for each domain state shown in Figure 2 can be used as a guide to EM interpretation in the discussion below.

2. Methods

The FORC measurements used in this study were all made with Princeton Measurements Corporation vibrating sample magnetometers in various laboratories around the world, with averaging times of 250 ms. The sample collections subjected here to FORC unmixing were treated with VARIFORC processing (Egli, 2013), where the parameters used are indicated in the respective figure captions for each data set presented.

While progressive reductive diagenesis might be expected to transform an initially more complex detrital/biogenic magnetic particle assemblage into one with simpler and less variable magnetic properties with either weak relict or authigenically enhanced magnetizations, we treat most sample sets independently. This approach maintains the integrity of the respective sample sets, and it recognises an important limitation associated with visualization of unmixing results. Multiple-component systems are readily represented in binary mixing lines, ternary diagrams, or in tetrahedra for quaternary mixtures, but higher-order mixing becomes more difficult to represent. This is not because of the mathematics, which can cope with many components, but because of the difficulty in visualizing results for so many components. Treating each sample set independently reduces the number of components identified, which helps to simplify data visualization.

2.1 The new FORC unmixing algorithm

PCA is used routinely in many disciplines to estimate unknown EMs by providing a low-rank approximation to data that facilitates definition of an empirical mixing space (Heslop, 2015). Details of FORC unmixing are described by Harrison et al. (2018); a brief outline is provided here to help readers to understand essential aspects of the approach. The principal advance in the FORC unmixing algorithm of Harrison et al. (2018) compared to that of Lascu et al. (2015) is that PCA is now performed on a representation of the magnetization curves rather than on processed FORC diagrams: this enables identification of both irreversible (i.e., remanence-bearing) and

reversible magnetization components so that the total magnetization is the sum of linearly additive components that satisfy the linear mixing equation. With this approach, contributions due to SP and MD components, which either have no or little irreversible magnetization, are recognised and quantified. With the graphical user interface available in FORCinel (Harrison & Feinberg, 2008), EMs can be visualized and selected interactively using the FORC-PCA algorithm. EM selection is not physically constrained and is based on user selection; best solutions are obtained when users have other constraints with which to "supervise" EM selection. To facilitate EM selection, newly devised feasibility metrics are included to define an unmixing space within which EMs are physically realistic (Harrison et al., 2018). The feasibility metrics are contoured to help users to select EMs that satisfy reasonable criteria such as requiring FORCs to change monotonically and to not cross each other. Demarcation of this physically realistic space helps users to avoid manual selection of unrealistic EMs. Even with these feasibility constraints, EM selection within the "allowable space" depends on the user. It is generally desirable to select EMs that lie close to measured data points, but an EM can also represent a mixture (e.g., Heslop, 2015), so it can be desirable to select an EM that lies further from measured data points to obtain a less mixed EM. These aspects of EM selection are subjective, which emphasizes the need for independent information about samples and the value of user expertise.

Smoothing of measurement noise is a key challenge for FORC processing (Roberts et al., 2000, 2014; Harrison & Feinberg, 2008; Egli, 2013). To ensure that results for EMs and individual samples are comparable, all samples within a given dataset are treated in the FORC-PCA approach with the same VARIFORC parameters. This poses particular challenges when studying diagenesis because signal/noise ratios will contrast strongly because sample sets tend to contain either typical detrital or diagenetically enhanced magnetic mineral assemblages along with diagenetically depleted assemblages. This issue is discussed below where relevant. Following Egli (2013), areas where the FORC distribution equals zero are white. The positive FORC signal is then scaled from

zero to the maximum value, and the negative region is scaled to its highest negative value. As discussed below, negative regions are important; more blue shades are evident when a negative region is deeper than for shallow negative regions.

While FORC unmixing has significant strengths, it also has limitations. The unmixing approach is as good as the data fed into it. For example, in the present study, FORC measurements focus on the <120 mT coercivity range. This biases explicitly against visualization of high coercivity minerals such as hematite and goethite. The weak spontaneous magnetizations of these minerals can also be swamped by more strongly magnetic co-existing minerals such as magnetite in FORC diagrams (e.g., Muxworthy et al., 2005; Roberts et al., 2014). Hematite tends to have broad coercivity spectra that extend from low to high values, so hematite will usually be partially evident in FORC diagrams with the field ranges used in this study (Roberts et al., 2006). As shown by Zhao et al. (2017), its detection can still be difficult when magnetite is present, and visualization of a hematite component is facilitated by use of adjustable non-linear color maps for FORC diagrams. Goethite has exceptionally high coercivity (Rochette et al., 2005), which makes it generally invisible in FORC diagrams in the adopted <120 mT coercivity range (cf. Roberts et al., 2006). Semi-quantitative determination of hematite and goethite concentrations is better achieved with low-temperature magnetic measurements (e.g., *Lagroix & Guyodo*, 2017). Our aim here is to understand diagenetic effects on typical detrital magnetic mineral assemblages and authigenic magnetic minerals that form during reductive diagenesis. Limitations associated with recognising hematite and goethite are acknowledged and readers with interests in understanding the diagenetic fate of these minerals should bear in mind that they will be largely invisible in the data representations in this paper. Overall, quantitative FORC analysis enabled by FORC unmixing has considerable potential because the domain state and interaction field distribution can be identified for each constituent magnetic component, which provides unprecedented levels of valuable information even for samples that comprise complex magnetic mixtures.

3. Samples and setting

We present here reanalysed FORC data from several of our own published studies of reductive magnetic mineral diagenesis. We use well studied sample sets so that the identified components are known and can be used as references for such diagenetic systems in future studies. The studied samples include modern depositional systems in which detrital/biogenic magnetic mineral assemblages at the seafloor undergo progressive magnetic property changes associated with down-core reductive dissolution. This type of environment is represented by hemipelagic sediments recovered in sediment cores CD143-55705 from the Oman margin, Arabian Sea (Rowan et al., 2009; Chang et al., 2016a) and LC13-81-G138 from the Northern California margin, Pacific Ocean (Rowan et al., 2009). These cores progress from the oxic to methanic diagenetic zones and are dominated by sulfidic diagenesis (see Figure 1 and Roberts (2015) for nomenclature). Sulfidic to methanic diagenetic systems with more complete diagenetic reduction are represented by tectonically uplifted marine sediments from Neogene sequences that crop out throughout eastern North Island, New Zealand (Rowan and Roberts, 2006), Pleistocene marine sediments from Crostolo River, Italy (Roberts et al., 2005), and middle Pleistocene alluvial sediments from a drill core on the Tiber River coastal plain near Rome, Italy (Florindo et al., 2007). Methanic environments are represented by sediment cores from Hydrate Ridge, Cascadia margin, offshore of Oregon, USA, which were recovered during Ocean Drilling Program (ODP) Leg 204 (Larrasoaña et al., 2007).

4. Results

4.1 Progressive down-core dissolution: ferruginous to sulfidic diagenesis

Many studies of coastal, hemipelagic, and pelagic sediments document progressive down-core diagenetic dissolution of detrital iron oxides in reducing environments (Karlin & Levi, 1983,

1985; Channell and Hawthorne, 1990; Karlin, 1990a, 1990b; Leslie et al., 1990a, 1990b; Roberts and Turner, 1993; Richter et al., 1999; Robinson et al., 2000; Yamazaki et al., 2003; Emiroglu et al., 2004; Liu et al., 2004; Garming et al., 2005; Rey et al., 2005; Riedinger et al., 2005; Dillon & Bleil, 2006; Kawamura et al., 2007; Rowan et al., 2009; Mohamed et al., 2011; Bouilloux et al., 2013; Roberts, 2015; Chang et al., 2016b). These studies provide a common picture of surface sediments, generally with all stages of organic matter diagenesis recognised in pore water profiles (Figure 1) (Roberts, 2015). Surface sediments generally contain trace abundances of detrital iron oxide minerals, including ferric oxyhydroxides and biogenic magnetite. With ongoing burial, reactive magnetic minerals start to undergo dissolution in ferruginous diagenetic environments and more pervasive dissolution occurs once sulfide is produced in pore waters, with the finest particles dissolving first, and pyrite becoming increasingly abundant in sulfidic environments. The depth at which the magnetic mineral content declines precipitously depends on the organic carbon content and sedimentation rate, and can vary significantly (e.g., Karlin & Levi, 1983; Kawamura et al., 2007; Roberts, 2015). We provide below two examples of FORC unmixing in environments that progress through the ferruginous and sulfidic diagenetic stages (Figure 1).

4.1.1 Core CD143-55705, Oman margin

FORC unmixing results are shown in Figure 3 for 50 samples from core CD143-55705. This core has been studied extensively in relation to magnetic mineral diagenesis (Rowan et al., 2009; Chang et al., 2016a) and is used here to illustrate diagenetic alteration of surface magnetic mineral assemblages. High initial IRM values (Figure 3j, gray curve) associated with a surface detrital/biogenic magnetic mineral assemblage decrease in two sharp steps at depths of ~2 m and ~4.2 m to low values below ~5 m. The large IRM contrast between the upper and lower parts of the core presents a challenge for calculating FORC distributions because of the variable signal/ noise ratio and the need to smooth FORCs more for weakly magnetized samples. This challenge is

illustrated in Figure 3a, b, where data are presented with respect to 3 principal components (PCs). In Figure 3a, data are plotted in the PC1-PC2 plane where it is clear that data from the upper part of the core (above ~4.2 m) fall on a single trend and data from the lower part of the core are scattered. Data that fall on a linear trend with positive PC1 values and near-zero PC2 values in Figure 3a for the upper part of the core define a triangular region in the PC1-PC3 plane in Figure 3b, where data from the lower part of the core (below ~4.2 m) are also scattered. Therefore, we treat separately data from the upper and lower parts of the core. The triangular region identified in the PC1-PC3 plane in Figure 3b is used to define a 3 EM system for the upper part of the core, where FORC diagrams for the 3 EMs are shown in Figure 3d-f and the vertices of the triangle that represent each EM are shown with respect to the data in Figure 3g. As should be the case for a physically meaningful solution, the triangle for the 3 EM mixing system falls within a broader zone enclosed by shaded contours (Figure 3g) in which FORCs increase monotonically without crossing each other (Harrison et al., 2018). Noisier data from the lower part of the core are treated separately and are represented in the PC1-PC2 plane in Figure 3h. The conventional unmixing procedure is to define a mixing region in PC space from which EMs are identified. Due to the noisy nature of the data, we chose a single component that represents the entire magnetic mineral assemblage for the lower part of the core. With this approach, the scatter in the PC1-PC2 plane is considered to be due to the noisy data for weakly magnetized samples rather than due to a mixed magnetic mineral assemblage. A FORC diagram for this component is shown in Figure 3i, which is represented by the point where PC1 and PC2 equal zero (Figure 3h). An equivalent approach would be to average all FORC measurements from this interval to improve the signal/noise ratio.

The three components identified in the upper part of core CD143-55705 (Figure 3d-f) are represented by a stable single domain (SD)/fine vortex state component (EM1), a coarse vortex state/MD component (EM2), where vortex states are identified following the arguments of Roberts et al. (2017), and a noisier superparamagnetic (SP) to SD component (EM3). Down-core

276 variations for the 3 components identified for the upper part of the core are shown in Figure 3j.
277 EM1 is dominant in the uppermost part of the core, where the sharp non-interacting central ridge
278 signal is interpreted to be due to biogenic magnetite (cf. Egli et al., 2010; Roberts et al., 2012).
279 EM1 also has a fine vortex state detrital contribution. Chang et al. (2016a) demonstrated that
280 biogenic and detrital magnetite record the low-temperature Verwey transition at different
281 temperatures and that biogenic magnetite is present in this core to depths of 4.60 m. This
282 interpretation is consistent with the down-core profile for EM1 in Figure 3j. EM2 represents a
283 coarser detrital magnetic mineral fraction whose relative importance increases to depths of ~4.6 m
284 at which point it drops sharply. EM3 is interpreted to represent an authigenic SP/SD component
285 that has trivial relative concentrations in the upper part of the core except for within the minimum
286 between two IRM peaks (Figure 3j). Its relative importance also increases sharply at ~4.6 m. The
287 contribution from EM1 drops at the base of the upper IRM peak and EM2 is responsible for all of
288 the lower IRM peak, and EM3 is always weak. The FORC diagram for EM3 (Figure 3f) is
289 indicative of an SP/SD greigite assemblage and is similar to the average FORC result for the lower
290 part of the core (Figure 3i), except that the latter has a greater stable SD contribution and a lesser
291 SP contribution. Interpretation of these trends in terms of diagenesis is discussed further below.
292
293 *4.1.2 Core LC13-81-G138, Northern California margin*
294 FORC unmixing results are shown in Figure 4 for core LC13-81-G138 (15 samples). This
295 core has also been studied previously in relation to magnetic mineral diagenesis (Rowan et al.,
296 2009). Contrasting magnetizations in the upper and lower, diagenetically depleted, parts of the
297 core mean that these two intervals are treated separately, as we did for core CD143-55705. Two
298 data clusters occur in the PC1-PC2 plane (Figure 4a): a tight cluster at PC1 $\approx 1 \times 10^{-4}$, and a noisy
299 one at PC1 < 0. In the PC1-PC3 plane (Figure 4b), the cluster at PC1 $\approx 1 \times 10^{-4}$ has a wider
300 distribution along a line at constant PC1 values. This trend defines a binary mixing line (Figure

4g) where EM1 is represented by a non-interacting stable SD component with a strong central ridge (Figure 4d) that is typical of biogenic magnetite (e.g., Egli et al., 2010; Roberts et al., 2012), and EM2 is a coarse detrital component dominated by the vortex state (Figure 4e). The measured data lie closer to EM2 and selection of EM1 in a position some distance away from the measured data (Figure 4g) is done to isolate an EM with a pure central ridge signature (Figure 4d) without admixture of EM2 (Figure 4e). Identical EM1 and EM2 components were identified by Channell et al. (2016), which they also identified as due to biogenic and detrital magnetite, respectively. Again, instead of fitting multiple components to the noisy FORC distributions from the lower part of the core, a single FORC distribution is selected to represent this interval (Figure 4f) where PC2 and PC3 equal zero (Figure 4c).

As is the case for core CD143-55705, the upper part of core LC13-81-G138 is dominated by SD biogenic and coarser detrital magnetite components. This biogenic component declines throughout the upper part of the record at the expense of the coarser detrital component in both cores LC13-81-G138 (Figure 4i) and CD143-55705 (Figure 3j). The diagenetically depleted lower part of core LC13-81-G138 (Figure 4f) has a similar average SP/SD FORC signature as the same zone in core CD143-55705 (Figure 3i). Interpretation of the LC13-81-G138 record in terms of diagenesis is discussed further in the Discussion section.

4.2 Magnetic enhancement via greigite authigenesis: sulfidic diagenesis

In the examples discussed above, reductive diagenesis has depleted initial surficial detrital/ biogenic magnetic mineral assemblages via dissolution, followed by weak magnetic enhancement via authigenic growth of SP/SD greigite. During early diagenesis, dissolved Fe^{2+} and H_2S react to form authigenic greigite, which can grow from initially fine SP/SD assemblages to stable SD particle assemblages with strong magnetostatic interactions that dominate magnetic mineral

assemblages. Greigite can also grow in methanic environments in association with AOM. We now consider greigite-forming environments with two sets of examples.

4.2.1 Greigite formation in Pleistocene sediments from Italy

4.2.1.1 Middle Pleistocene alluvial sediments, Tiber River plain

We present results here for Middle Pleistocene alluvial sediments from a drill core on the Tiber River plain near Rome, Italy (Florindo et al., 2007). Harrison et al. (2018) used FORC results from this group of 16 samples to illustrate FORC unmixing, which we show in Figure 5. Three EMs are identified, all of which are due to greigite. EM1 (Figure 5a) has less vertical spread than EM2 (Figure 5b), and a negative peak that starts from below the main positive peak of the FORC distribution with a trend at –45° from the positive peak (Figure 5a). EM2 has a strong positive contribution with a broad, concentric distribution, and a deeper negative contribution along the negative B_i axis (Figure 5b) that is typical of interacting SD greigite (Roberts et al., 2006, 2011). EM3 comprises a SP/SD component (Figure 5c) that is present in all sample sets analysed here. FORC measurements for 4 weakly magnetized samples were averaged to increase the signal/noise ratio to obtain an average result that was included in the PCA to identify EM3. The identified three-EM system is defined within the contoured region for physically realistic solutions in the PC1-PC2 plane (Figure 5d). Typical FORC diagrams for real samples are shown for comparison with the calculated EMs in Figure 5e-h. These samples are dominated by EM2 (Figure 5g, 5h), but also clearly represent mixtures with the other EMs (Figure 5e, 5f). Details of the EMs and the processes that they represent are discussed further below.

This example also illustrates challenges associated with FORC unmixing. The horizontal stripes in FORC diagrams for EM2 and EM3 are due to VARIFORC smoothing (Egli, 2013), where the unmixing space is defined using noisy experimental data and the same VARIFORC parameters are used to unmix the entire sample set (Harrison et al., 2018). These “stripes” are

mostly present in weak samples or EMs. The weak EM3 is dominated by a horizontal ridge; measurement noise coupled with the chosen VARIFORC parameters produces the artefact stripes. Despite the visually and technically unappealing artefact stripes associated with FORC smoothing for weakly magnetized samples and calculated EMs, the overall FORC pattern is clear. Smoothing of noisy measurement data is a key challenge in FORC data processing (e.g., Roberts et al., 2000, 2014; Harrison and Feinberg, 2008; Egli, 2013); this example illustrates some of the compromises associated with the second derivative calculation used to obtain FORC distributions.

4.2.1.2 Lower Pleistocene marine sediments, Crostolo River

We present results here for tectonically uplifted Lower Pleistocene greigite-bearing marine sediments from Crostolo River, Italy (Tric et al., 1991; Roberts et al., 2005). Three EMs are identified from 12 analysed samples (Figure 6a-c), which are similar to those from the Tiber River plain, with two distinct interacting SD components (EM1 and EM2; Figure 5a, 5b) and one SP/SD component (EM3; Figure 5c). In PC1-PC2 space, most data points cluster around EM2 (Figure 6e), so that measured FORC diagrams are mainly like those of EM2 (Figure 6f). Only four data points reveal more scatter (Figure 6d, e); these samples represent mixtures of the three identified EMs, where sample CR01B (Figure 6i) is a mixture of EM1 and EM2, sample CR03B is closer to EM1 (Figure 6g), and sample CR02D lies closest to EM3 but has contributions from both EM1 and EM2 (Figure 6h). Like the Tiber River plain example, the three EMs are all authigenic components that grew during diagenesis, as discussed further below.

4.2.2 Greigite formation in Neogene marine sediments, New Zealand

We present results here for tectonically uplifted Neogene marine sediments that crop out throughout eastern New Zealand (Rowan and Roberts, 2006). We group FORC results for 129 samples from wide-ranging mudstone outcrops of varying age because they appear to have

undergone diagenesis in similar environments. Four EMs are identified from FORC unmixing (Figure 7). These sediments have been altered strongly by reductive diagenesis, but a detrital magnetic component persists in some tuffaceous samples, and iron-titanium oxides are also likely to occur as inclusions within detrital silicate particles (Chang et al., 2016c). EM1 is identified as a coarse detrital iron oxide MD component carried by four tuffaceous samples from the NR locality of Rowan and Roberts (2006) (Figure 7a). By contrast, EM2 is represented by pure SD greigite with strong magnetostatic interactions (Figure 7b) that is a typical signature of authigenic greigite (e.g., Roberts et al., 2006, 2011; Rowan & Roberts, 2006; Florindo et al., 2007; Vasiliev et al., 2007; Chang et al., 2014; Liu et al., 2016). EM3 and EM4 link the other two components (Figure 7e, f), where both have a strong SP signal but EM3 contains a SD/vortex state detrital fraction (Figure 7c), while EM4 comprises a less strongly interacting SP/SD greigite component (Figure 7d). These four components are typical of the New Zealand sediments studied by Rowan and Roberts (2006). Mixing among the four EMs is illustrated in Figure 7e and 7f, and FORC diagrams for typical samples with intermediate properties are shown in Figure 7g-7j. Details of the EMs and the processes that they represent are discussed further below.

4.3 Magnetic mineral diagenesis in methanic environments

Methanic environments are represented by sediment cores from Hydrate Ridge, Cascadia margin, offshore of Oregon, USA, which were recovered during ODP Leg 204 (Larrasoaña et al., 2007). FORC diagrams for 20 samples can be represented by four components (Figure 8), the first three of which are common to sulfidic environments (Figures 5, 6). EM1 is a coarse vortex state component due to detrital magnetic minerals (Figure 8a), which is associated with terrigenous inputs via turbidites (Larrasoaña et al., 2007). EM2 is a strongly magnetostatically interacting SD greigite component (Figure 8b), while EM3 corresponds to the authigenic SP/SD component that is seen in all examples above (Figure 8c). EM4 (Figure 8d) is typical of methanic environments,

and is due to authigenic pyrrhotite (e.g., Weaver et al., 2002; Larrasoaña et al., 2007; Roberts et al., 2010; Kars & Kodama, 2015a, b; Horng, 2018). Relationships among the EMs for this data set are shown in Figure 8e, 8f. Typical FORC diagrams for intermediate samples that fall between EMs are shown in Figure 8g, 8h. The EM2-EM3 trend represents the dominant variation between fine SP/SD greigite and stable SD greigite assemblages. EM1 represents an isolated component where coarse detrital particles have been admixed via exogenous turbidite inputs, while EM4 represents an additional authigenic pyrrhotite component that has formed during methanic diagenesis. Details of the EMs and the processes that they represent are discussed further below.

5. Discussion

5.1 Domain states and magnetocrystalline anisotropy types in EMs

Expected FORC signatures for all domain states (Figure 2) can be compared with those identified for each EM in Figures 3-8. When using PCA, any EM can represent a mixture of magnetic components (Heslop, 2015), and various EMs evidently consist of such mixtures (e.g., EM1 in Figure 3; EM3 in Figure 7). Nevertheless, the domain states represented by each EM are understandable in terms of the framework provided in Figure 2. In addition to recognising domain states, FORC results can reveal features related to the type of magnetic anisotropy that controls the magnetization in different minerals. For example, SD particles with uniaxial anisotropy always have a negative peak along the B_i axis (Muxworthy et al., 2004; Newell, 2005). Harrison & Lascu (2014) demonstrated that FORC distributions for SD particles with cubic anisotropy also have such a peak (feature 1 in Figure 5f) as well as an additional negative peak below the main positive peak with elongation at –45° (feature 2 in Figure 5f). Such negative elongated peaks can be obscured by various features, including mixtures of domain states and strong magnetostatic interactions (Harrison & Lascu, 2014), but when they are present they indicate the presence of magnetic particles with multi-axial rather than uniaxial anisotropy. The presence of negative peaks

such as feature 2 in Figure 5f in greigite-bearing samples and EMs as documented here (Figure 5a) confirms that greigite has cubic magnetocrystalline anisotropy (Roberts, 1995; Roberts et al., 2011). This type of negative peak is also seen systematically in FORC diagrams for authigenic pyrrhotite (Figure 8d, 8g) that forms in methanic environments (e.g., Weaver et al., 2002; Larrasoaña et al., 2007; Roberts et al., 2010; Kars & Kodama, 2015a, b; Horng, 2018). This is due to triaxial anisotropy in the basal plane of pyrrhotite crystals (Martín-Hernández et al., 2008). Such features provide diagnostic information about magnetocrystalline anisotropy type, which is relevant to magnetic mineral identification, in addition to providing information about domain state. Importantly, even though pyrrhotite and greigite give rise to negative peaks with elongation at –45°, FORC distributions for authigenic pyrrhotite typically have lower coercivity and negative slopes (Figures 6a, 6g, 7j, 8d, 8g) than those for greigite (Figure 5a, 5f).

5.2 Diagenetic processes and interpretation of FORC unmixing results

The EMs identified in the above examples from well-studied settings provide a consistent and systematic view of the magnetic properties associated with different diagenetic zones and of well documented diagenetic processes in these reducing sediments. Linking these characteristic FORC results to diagenetic processes (Figure 9) should assist future studies of sediments that have undergone similar magnetic mineral diagenesis. Below we outline the main magnetic properties and diagenetic processes that affect magnetic minerals in the oxic to ferruginous, sulfidic, and methanic zones (Figure 9), respectively.

5.2.1 Oxic to ferruginous diagenesis

Surficial seafloor, lake bed, or river bed sediments are likely to contain primary magnetic mineral assemblages with relatively little diagenetic modification, especially if bottom waters are oxic. Compared to the pervasive diagenetic modification of magnetic minerals that occurs in the

sulfidic and methanic zones, modification of magnetic minerals is relatively minor in the oxic, nitrogenous, and manganous zones and starts to become more significant in the ferruginous zone (Roberts, 2015). Cores CD143-55705 and LC13-81-G138 lack pore water chemistry data, but a diagenetic zonation can be developed by combining FORC results with the scanning electron microscope (SEM) observations of Rowan et al. (2009) and the SEM and transmission electron microscope (TEM) observations of Chang et al. (2016a) because observed biogenic and authigenic minerals can be linked to the biogeochemistry of sedimentary environments (Berner, 1981).

Addition of biogenic magnetite to primary detrital magnetic mineral assemblages contributes significantly to the magnetic properties of surface sediments in cores CD143-55705 and LC13-81-G138. Magnetotactic bacteria generally biomineralize magnetite at the base of the nitrogenous zone (Figure 9), which may occur in the water column or uppermost sediment column, where iron is bioavailable due to upward diffusion of dissolved Fe^{2+} from the underlying ferruginous zone (Roberts, 2015). Contributions from the inorganic post-mortem remains of magnetotactic bacteria are evident from a central ridge signature (Figures 3d, 4d) in FORC diagrams (Egli et al., 2010; Roberts et al., 2012) from the uppermost sediments in cores CD143-55705 and LC13-81-G138 (Figure 9). TEM observations (Chang et al., 2016a) demonstrate the presence of fossil magnetosomes in these surficial sediments and confirm our interpretation of the central ridge FORC signature. Fine-grained bacterial magnetite is highly reactive under reducing conditions and EM1 is depleted progressively with depth in both cores (Figures 3j, 4i). This loss of the finest magnetite population can occur in association with iron reduction in the ferruginous diagenetic zone or with sulfate reduction in the sulfidic zone, and enhances the contribution of a coarser EM2 vortex state/MD component (Figures 3j, 4i). Chang et al. (2016a) demonstrated that detrital and biogenic magnetite have different Verwey transition temperatures and used this to demonstrate that biogenic magnetite persists to depths of ~4.6 m in core CD143-55705 at which point the IRM is depleted to low values. From SEM observations, Rowan et al. (2009)

documented minor sedimentary pyrite at depths of 0.1 m below the top of core CD143-55705, which indicates that sulfidic conditions were established close to the sediment-water interface (cf. Berner, 1981), and that the overlying diagenetic zones must be extremely thin. Both studied sediment cores occur in regions with an oceanic oxygen minimum zone (OMZ), but were both taken from below the modern OMZ (Levin, 2003). Bottom waters in these settings are oxic and the rapid progression to sulfidic conditions at shallow depths is likely due to high organic carbon inputs and microbial respiration of this organic matter near the sediment-water interface. Oxic to ferruginous diagenetic zones in the studied cores are likely to have been present because upward diffusion of bioavailable Fe^{2+} from the ferruginous zone is likely to have been used by magnetotactic bacteria to biomineralize magnetite at the base of the nitrogenous zone. Nevertheless, these zones would have been thin considering the shallow depths at which pyrite is present in these sediments. All further magnetic mineral diagenesis in these cores will have occurred under sulfidic or methanic conditions, as discussed below.

5.2.2 Sulfidic diagenesis

Dissolution of magnetite and hematite becomes ubiquitous in sulfidic sediments (Canfield and Berner, 1987). Dissolved Fe^{2+} released from detrital and biogenic iron-bearing minerals reacts with dissolved H_2S, which is a by-product of sulfate reduction, to form sedimentary iron sulfides, particularly pyrite (Berner, 1984). Dissolution of detrital magnetite and hematite during sulfidic diagenesis, and replacement by paramagnetic pyrite, which does not carry a permanent magnetization, progressively destroys the primary paleomagnetic record. Hematite is less reactive than magnetite in reducing environments (Robinson et al., 2000; Yamazaki et al., 2003; Emiroglu et al., 2004; Liu et al., 2004; Garming et al., 2005; Rey et al., 2005; Kawamura et al., 2007; Rowan et al., 2009; Roberts, 2015; Korff et al., 2016), but it will also undergo progressive dissolution with depth. We do not discuss the fate of hematite further in this context because it is

less visible in FORC diagrams than magnetite (see Section 2.1 above). Progressive loss of detrital and biogenic magnetic minerals via dissolution and pyrite formation is evident in the upper parts of cores CD143-55705 and LC13-81-G138 (Figures 3j, 4i). The presence of pyrite at shallow depths in core CD143-55705 (Rowan et al., 2009; Chang et al., 2016a) indicates that sulfidic conditions existed just below the sediment-water interface, which raises the question of why surficial IRM values decrease to low values down-core in two steps rather than one (Figures 3j) in core CD143-55705. The lower IRM peak is depleted in biogenic magnetite (EM1) and is enriched in the coarser vortex state/MD detrital component (EM2). In core CD143-55705, there is a local increase in the diagenetic SP/SD greigite component (EM3) in the minimum between IRM peaks. EM3 is then the only component below the lower IRM peak. These features indicate that the base of the upper IRM peak represents the modern sulfate-methane transition (SMT; Figure 9). The base of the lower IRM peak likely represents a former SMT position, which migrated upward with a change in sedimentary conditions to leave a relict coarse detrital component (EM2) between the old and new sulfidic dissolution fronts (Riedinger et al., 2005; Rowan et al., 2009). Even though biogenic magnetite is fine-grained and reactive to dissolved sulfide, low-temperature magnetic measurements indicate that minor magnetofossil concentrations remain in core CD143-55705 to depths of ~4.6 m in correspondence with the former SMT position (Chang et al., 2016a).

Once detrital and biogenic magnetic components have been dissolved by sulfidic diagenesis, the only magnetic minerals that are likely to remain are authigenic minerals that form in reducing environments, relict minerals that are unreactive or slowly reactive to sulphide, such as chromite (Hounslow, 1996), titanohematites (Franke et al., 2007; Garming et al., 2007), or iron oxide inclusions within silicate minerals that are protected from sulfidization by their silicate hosts (Roberts, 2015; Chang et al., 2016b, 2016c). The only component detected with FORC unmixing below the former SMT position at ~4.6 m in core CD143-55705 (Figure 3i) is an authigenic SP/SD greigite component (EM3). This component is fine-grained, weak, and lacks strong

magnetostatic interactions. It is possible that the magnetically non-interacting SD part of EM3 (Figure 3i, 4f) is a central ridge signature (Egli et al., 2010) associated with greigite-bearing magnetotactic bacteria. Identification of ancient magnetite magnetofossils has expanded greatly with joint use of FORC diagrams and TEM observations (e.g., Yamazaki, 2008, 2009; Roberts et al., 2012; Yamazaki & Ikehara, 2012). Roberts (2015) suggested that greigite magnetofossils should be more abundant in the geological record than magnetite magnetofossils, particularly if they are gradient organisms (Bazylinski & Frankel, 2004) that live near the so-called oxic-anoxic interface (i.e., nitrogenous to ferruginous boundary in Figure 1), because magnetite dissolves when buried into the sulfidic diagenetic zone, whereas greigite remains stable. The potential for widespread greigite magnetofossil occurrences remains undemonstrated, and is an important research avenue. The link between central ridge FORC signatures and greigite magnetofossils is established (Reinholdsson et al., 2013; Chang et al., 2014; Chen et al., 2014), but the challenge will be to provide convincing evidence from TEM observations of greigite magnetosomes, which do not have the ideal crystal morphology or chain arrangement of magnetite magnetosomes (Farina et al., 1990; Mann et al., 1990; Pósfai et al., 1998a, 1998b; Kasama et al., 2006).

Greigite formation has been documented in modern continental margin marine sediments at depths of several meters to tens of meters below the sediment-water interface (Kasten et al., 1998; Jørgensen et al., 2004; Liu et al., 2004; Neretin et al., 2004; Riedinger et al., 2005, 2014; Larrasoaña et al., 2007; Fu et al., 2008; Rowan et al., 2009). Strongly magnetized stable SD greigite with strong magnetostatic interactions that is typically associated with sulfidic diagenesis (EM2 in Figures 5-8) is not evident in the relatively short sediment cores discussed here. There is, therefore, a disconnect in our understanding of early diagenesis and the point at which the strongly interacting stable SD greigite grows. It has been assumed that initial SP/SD greigite assemblages (EM3 in Figure 3-8) continue to grow through the stable SD blocking volume with progressive sulfidization at depth to transform into such assemblages (Rowan and Roberts, 2006; Rowan et al.,

2009), but marine sediment cores are usually not long enough to assess whether this progressive greigite formation mechanism is correct. Liu et al. (2016) documented strongly interacting stable SD greigite in discrete sediment layers from a long sediment core from the South Yellow Sea starting from depths of ~6 m below the sediment-water interface. However, this shallow water setting has been subjected to major non-steady state diagenetic changes associated with large-amplitude Quaternary sea level variations and lack of a pore-water profile makes it difficult to assess the diagenetic environment in which this greigite formed. Stable SD greigite has been documented extensively within sediments in methanic environments in association with AOM (Housen & Musgrave, 1996; Horng & Chen, 2006; Musgrave et al., 2006; Enkin et al., 2007; Larrasoaña et al., 2007; Kars & Kodama, 2015a, b; Shi et al., 2017), so the possibility of greigite formation in either the sulfidic or methanic zones should be considered (Figure 9). The depth of this greigite formation has important consequences for the timing of sedimentary paleomagnetic signal acquisition. Rowan et al. (2009) estimated from widely distributed sediment cores that the onset of early greigite formation at the SMT (with properties like EM3) starts from 0.6 to >220 kyr after deposition depending on the sedimentation rate, with SD greigite formation in underlying sediments occurring over periods of ≥1 to ≥160 kyr. Later formation in the methanic zone can lead to remanence acquisition delays of a few kyr to Myr (Larrasoaña et al., 2007), including complete remagnetization (Roberts and Weaver, 2005). Assessing recording delays associated with greigite growth is a key issue in magnetic studies of diagenetically reduced sediments.

5.2.3 Methanic diagenesis

In the methanic diagenetic zone, AOM is the most important known process that affects magnetic mineral assemblages (Roberts, 2015). Sulfate reduction via AOM consumes pore water methane and sulfate to depletion at the SMT (Figure 1) and provides a secondary, relatively mobile, source of H_2S (Murray et al., 1978; Devol & Ahmed, 1981; Niewöhner et al., 1998;

575 Kasten & Jørgensen, 2000; Jørgensen & Kasten, 2006) that can cause both reductive dissolution of
576 detrital iron oxides and formation of secondary ferrimagnetic iron sulfides. If the SMT occurs at
577 shallow depths, as in the examples shown in Figures 3 and 4, early diagenetic greigite growth will
578 result in relatively short delays in paleomagnetic signal acquisition. If Fe^{2+} and H_2S are available
579 at greater depths (Figure 9), however, greigite can form at any time during diagenesis (Roberts
580 and Weaver, 2005). Fe^{2+} concentrations can increase within the methanic zone due to coupling of
581 AOM to Fe and Mn reduction (Beal et al., 2009; Sivan et al., 2011; Segarra et al., 2013; Riedinger
582 et al., 2014; Egger et al., 2015). While dissolved sulfide production is expected at the SMT during
583 steady-state diagenesis (Figure 1), methane is often mobilized through fracture and fault networks
584 in tectonically active settings. AOM of this mobile methane can release H_2S that will react with
585 any available Fe^{2+} to cause magnetic iron sulfide formation at any time during diagenesis (Figure
586 9), which makes AOM an important process in magnetic mineral diagenesis. Greigite is known to
587 occur in methane-rich sediments or in methane hydrates (e.g., Housen and Musgrave, 1996; Horng
588 and Chen, 2006; Musgrave et al., 2006; Enkin et al., 2007), while greigite and pyrrhotite also form
589 in association with methane diffusion (Figures 5, 8, 9; Larrasoaña et al., 2007).

590 Potential greigite formation during both sulfidic and methanic diagenesis (Figure 9) raises
591 questions about the diagenetic zone in which the stable SD greigite formed in the case studies
592 illustrated in Figures 5-8. The presence of greigite in methanic environments is generally
593 associated with its formation during earlier sulfidic diagenesis, but this is not necessarily the case.
594 The common occurrence of remagnetizations in greigite-bearing sediments of eastern North
595 Island, New Zealand, led Rowan and Roberts (2008) to suggest that late greigite formation was
596 associated with deeper diagenetic processes such as gas hydrate formation and AOM. Likewise,
597 van Dongen et al. (2007) demonstrated from organic geochemical evidence that AOM occurred
598 within greigite-bearing nodules. Nevertheless, assumed linkages between greigite formation and
599 sulfidic environments have not been questioned widely. In addition to greigite, pyrrhotite has been

600 documented widely in association with methane hydrates (Housen and Musgrave, 1996; Horng
601 and Chen, 2006; Musgrave et al., 2006; Enkin et al., 2007; Rudmin et al., 2018) and in tectonically
602 fractured areas that support active methane diffusion or venting (Larrasoaña et al., 2007), which
603 suggests that authigenic pyrrhotite is an indicator of methanic environments (Figure 9). The
604 authigenic pyrrhotite that forms in methanic environments is magnetic so it has been assumed
605 widely to be monoclinic pyrrhotite (e.g., Weaver et al., 2002; Larrasoaña et al., 2007; Kars &
606 Kodama, 2015a; Roberts, 2015). Horng (2018) and Horng and Roberts (2018) demonstrated
607 recently that authigenic pyrrhotite in methanic sediments has an unambiguous hexagonal rather
608 than monoclinic crystal structure. Hexagonal pyrrhotite is expected to be antiferromagnetic, so
609 further work is needed to understand and explain its magnetic structure.

610 The above observations raise the question of whether sulfidic and methanic diagenetic
611 environments can be distinguished from each other from the magnetic properties of magnetic
612 mineral assemblages. Characteristic kidney-shaped FORC distributions with negative slopes for
613 SD pyrrhotite and a negative region also with negative slope (Weaver et al., 2002; Wehland et al.,
614 2005; Larrasoaña et al., 2007; Roberts et al., 2010; Kars & Kodama, 2015a, b; Horng, 2018)
615 suggest that pyrrhotite can be identified readily from FORC distributions (Figure 8d, 8g). This
616 negative region is sometimes not evident because of the scaling of FORC diagrams, but it can be
617 made more visible through manual adjustment of the color scale. Nevertheless, the negative slope
618 of the positive part of FORC distributions for pyrrhotite-bearing samples is distinct from FORC
619 distributions for greigite-bearing samples. Additionally, the peak coercivity of FORC distributions
620 for our SD greigite-bearing samples is ~60-70 mT, while it is ~20-40 mT for our pyrrhotite-
621 bearing samples. Based on these observations, we suggest that the Crostolo River sediments
622 contain previously unidentified pyrrhotite (Figures 6a, 6g, 6h). In contrast, Tric et al. (1991)
623 argued that the Crostolo Rover sediments contain a detailed Upper Olduvai polarity transition
624 record associated with greigite that grew during earliest burial. Roberts et al. (2005) demonstrated

from detailed SEM observations that different generations of greigite formed in these sediments, but they could not constrain the timescales involved and concluded that it was relatively early. Thus, these sediments record magnetic signatures associated with both sulfidic and methanic stages, which illustrates the potential difficulties in discriminating in which of these two stages greigite formed. Magnetic signatures due to pyrrhotite have not been detected previously in the Crostolo River sediments, which provides new information about the diagenetic history of these sediments. It is important to note that pyrrhotite is not always identified in association with methane hydrates (e.g., Shi et al., 2017). Also, even though remagnetization of sediments from eastern North Island, New Zealand, has been attributed to tectonically driven methane migration (Rowan & Roberts, 2008), no pyrrhotite is evident in FORC diagrams from these sediments (Figure 7). However, pyrrhotite FORC signatures are evident in four samples from the NC locality (Figure 7j) in northeastern South Island (Rowan & Roberts, 2006), which indicates that these sediments experienced methanic diagenesis. Overall, though, key markers for diagenetic processes of interest may not always be present. As ever, positive evidence is important and an absence of evidence provides neither confirmation nor disproof of a process.

6. Conclusions

FORC unmixing with PCA provides clear detection of magnetic properties associated with magnetic mineral diagenesis during early sediment burial. From our analysis of multiple data sets (FORC measurements for > 240 samples), consistent magnetic components are identified from sediments that have undergone various stages of reductive diagenesis (Figure 9). Relatively unaltered magnetic assemblages in oxic to manganous diagenetic zones are rich in coarse detrital magnetic minerals and fine biogenic magnetite. These minerals dissolve progressively in ferruginous and sulfidic diagenetic environments and largely disappear when buried to the base of the sulfidic zone at the SMT. Below the SMT, authigenic phases dominate magnetic mineral

assemblages. An initial weak and magnetostatically weakly interacting authigenic SP/SD greigite component is identified in all studied sulfidic and methanic settings, along with stable and strongly interacting SD greigite. An additional magnetostatically interacting pyrrhotite component is identified in methanic environments. Mixtures of the components are common in the respective environments; FORC unmixing enables quantification of the contributions of each component. Identification of FORC signatures for each component and association of their magnetic properties with the diagenetic processes to which they have been subjected provides information concerning sedimentary magnetic signatures that will enable researchers to grapple with relevant questions that arise when considering diagenesis and its effects on paleomagnetic and environmental signals.

Despite the clarity of our results concerning the magnetic mineral components that occur in reducing diagenetic environments, our work raises a key unresolved question. Greigite can form in both sulfidic and methanic diagenetic environments (Figure 9); in most cases where greigite has been identified, it remains unknown in which of these diagenetic zones greigite formed. Significant smoothing can affect paleomagnetic and environmental signal acquisition in both cases, but smoothing will be a more significant complication in deeper methanic environments. Determining the environment in which greigite formed is important for understanding magnetic signals associated with sedimentary reductive diagenetic processes. It is important to gain a better understanding in future studies of the extent to which stable SD greigite grows in sulfidic versus methanic diagenetic environments. It is also important to note that authigenic pyrrhotite forms in methanic environments, so it will usually record a delayed paleomagnetic signal.

Acknowledgements

This work was supported financially by the Australian Research Council through grant DP160100805, by the European Research Council under the European Union's Seventh Framework Programme (FP/2007–2013)/ERC grant agreement number 320750, and by National

675 Institute of Advanced Industrial Science and Technology, Ministry of Economy, Trade and
676 Inustry, Japan. We thank Luca Lanci and Tilo von Dobeneck for constructive reviews that
677 improved this paper, Michael Walter for editorial handling, and Mrs Sue Wigley for organizing a
678 writing week that enabled the first five authors of this paper to finalize the unmixing algorithm
679 and prepare manuscripts for publication. The authors are in the process of creating a global FORC
680 database to which the data presented in this paper will be added after publication.
681

682 **References**

683 Bazylinski, D. A., & Frankel, R. B. (2004). Magnetosome formation in prokaryotes. *Nature*
684 *Reviews Microbiology*, *2*, 217–230.
685 Beal, E. J., House, C. H., & Orphan, V. J. (2009). Manganese- and iron-dependent marine
686 methane oxidation. *Science*, *325*, 184–187.
687 Berner, R. A. (1981). A new geochemical classification of sedimentary environments. *Journal of*
688 *Sedimentary Petrology*, *51*, 359–365.
689 Berner, R. A. (1984). Sedimentary pyrite formation: An update. *Geochimica et Cosmochimica*
690 *Acta*, *48*, 605–615.
691 Bouilloux, A., Valet, J. P., Bassinot, F., Joron, J. L., Blanc-Valleron, M. M., Moreno, E., Dewilde,
692 F., Kars, M., & Lagroix, F. (2013). Diagenetic modulation of the magnetic properties in
693 sediments from the Northern Indian Ocean. *Geochemistry, Geophysics, Geosystems*, *14*, 3779–
694 3800.
695 Canfield, D. E., & Berner, R. A. (1987). Dissolution and pyritization of magnetite in anoxic
696 marine sediments. *Geochimica et Cosmochimica Acta*, *51*, 645–659.
697 Canfield, D. E., & Thamdrup, B. (2009). Towards a consistent classification scheme for
698 geochemical environments, or, why we wish the term ‘suboxic’ would go away. *Geobiology*, *7*,
699 385–392.

Carvallo, C., Roberts, A. P., Leonhardt, R., Laj, C., Kissel, C., Perrin, M., & Camps, P. (2006). Increasing the efficiency of paleointensity analyses by selection of samples using first-order reversal curve (FORC) diagrams. *Journal of Geophysical Research: Solid Earth*, *111*, B12103, doi:10.1029/2005JB004126.

Chang, L., Vasiliev, I., van Baak, C., Krijgsman, W., Dekkers, M. J., Roberts, A. P., Fitz Gerald, J. D., van Hoesel, A., & Winklhofer, M. (2014). Identification and environmental interpretation of diagenetic and biogenic greigite in sediments: A lesson from the Messinian Black Sea. *Geochemistry, Geophysics, Geosystems*, *15*, 3612–3627.

Chang, L., Heslop, D., Roberts, A. P., Rey, D., & Mohamed, K. J. (2016a). Discrimination of biogenic and detrital magnetite through a double Verwey transition temperature. *Journal of Geophysical Research: Solid Earth*, *121*, 3–14.

Chang, L., Bolton, C. T., Dekkers, M. J., Hayashida, A., Heslop, D., Krijgsman, W., Kodama, K., Paterson, G. A., Roberts, A. P., Rohling, E. J., Yamamoto, Y., & Zhao, X. (2016b). Asian monsoon modulation of nonsteady state diagenesis in hemipelagic marine sediments offshore of Japan. *Geochemistry, Geophysics, Geosystems*, *17*, 4383–4398.

Chang, L., Roberts, A. P., Heslop, D., Hayashida, A., Li, J. H., Zhao, X., Tian, W., & Huang, Q. H. (2016c). Widespread occurrence of silicate-hosted magnetic mineral inclusions in marine sediments and their contribution to paleomagnetic recording. *Journal of Geophysical Research: Solid Earth*, *121*, 8415–8431.

Channell, J. E. T., & Hawthorne, T. (1990). Progressive dissolution of titanomagnetites at ODP Site 653 (Tyrrhenian Sea). *Earth and Planetary Science Letters*, *96*, 469–480.

Channell, J. E. T., Harrison, R. J., Lascu, I., McCave, I. N., Hibbert, F. D., & Austin, W. E. N. (2016). Magnetic record of deglaciation using FORC-PCA, sortable-silt grain size, and magnetic excursion at 26 ka, from the Rockall Trough (NE Atlantic). *Geochemistry, Geophysics, Geosystems*, *17*, 1823–1841.

Chen, A. P., Berounsky, V. M., Chan, M. K., Blackford, M. G., Cady, C., Moskowitz, B. M., Kraal, P., Lima, E. A., Kopp, R. E., Lumpkin, G. R., Weiss, B. P., Hesse, P., & Vella, N. G. F. (2014). Magnetic properties of uncultivated magnetotactic bacteria and their contribution to a stratified estuary iron cycle. *Nature Communications*, *5*, 4797, doi:10.1038/ncomms5797.

Chen, L., Heslop, D., Roberts, A. P., Chang, L., Zhao, X., McGregor, H. V., Marino, G., Rodriguez-Sanz, L., Rohling, E. J., & Pälike, H. (2017). Remanence acquisition efficiency in biogenic and detrital magnetite and recording of geomagnetic paleointensity. *Geochemistry, Geophysics, Geosystems*, *18*, 1435–1450.

Devol, A. H., & Ahmed, S. I. (1981). Are high rates of sulphate reduction associated with anaerobic oxidation of methane? *Nature*, *291*, 407–408.

Dillon, M., & Bleil, U. (2006). Rock magnetic signatures in diagenetically altered sediments from the Niger deep-sea fan. *Journal of Geophysical Research: Solid Earth*, *111*, B03105, doi:10.1029/2004JB003540.

Egger, M., Rasigraf, O., Sapart, C. J., Jilbert, T., Jetten, M. S. M., Röckmann, T., van der veen, C., Bânda, N., Kartal, B., Ettwig, K. F., & Slomp, C. P. (2015). Iron-mediated anaerobic oxidation of methane in brackish coastal sediments. *Environmental Science and Technology*, *49*, 277–283.

Egli, R. (2004a). Characterization of individual rock magnetic components by analysis of remanence curves, 1. Unmixing natural sediments. *Studia Geophysica et Geodetica*, *48*, 391–446.

Egli, R. (2004b). Characterization of individual rock magnetic components by analysis of remanence curves, 2. Fundamental properties of coercivity distributions. *Physics and Chemistry of the Earth*, *29*, 851–867.

748 Egli, R. (2004c). Characterization of individual rock magnetic components by analysis of
749 remanence curves. 3. Bacterial magnetite and natural processes in lakes. *Physics and*
750 *Chemistry of the Earth*, *29*, 869–884.
751 Egli, R. (2013). VARIFORC: An optimized protocol for calculating non-regular first-order
752 reversal curve (FORC) diagrams. *Global and Planetary Change*, *110*, 302–320.
753 Egli, R., Chen, A. P., Winklhofer, M., Kodama, K. P., & Horng, C. S. (2010). Detection of
754 noninteracting single domain particles using first-order reversal curve diagrams.
755 *Geochemisry, Geophysics, Geosystems, 11*, Q01Z11, doi:10.1029/2009GC002916.
756 Emiroglu, S., Rey, D., & Petersen, N. (2004). Magnetic properties of sediment in the Ria de
757 Arousa (Spain): Dissolution of iron oxides and formation of iron sulphides. *Physics and*
758 *Chemistry of the Earth*, *29*, 947–959.
759 Enkin, R. J., Baker, J., Nourgaliev, D., Iassonov, P., & Hamilton, T. S. (2007). Magnetic
760 hysteresis parameters and Day plot analysis to characterize diagenetic alteration in gas
761 hydrate bearing sediments. *Journal of Geophysical Research: Solid Earth*, *112*, B06S90.
762 http://dx.doi.org/10.1029/2006JB004638.
763 Farina, M., Esquivel, D. M. S., & Lins de Barros, H. G. P. (1990). Magnetic iron-sulphur crystals
764 from a magnetotactic microorganism. *Nature*, *343*, 256–258.
765 Florindo, F., Karner, D. B., Marra, F., Renne, P. R., Roberts, A. P., & Weaver, R. (2007).
766 Radioisotopic age constraints for Glacial Terminations IX and VII from aggradational
767 sections of the Tiber River delta in Rome, Italy. *Earth and Planetary Science Letters*, *256*,
768 61–80.
769 Franke, C., Pennock, G. M., Drury, M. R., Engelmann, R., Lattard, D., Garming, J. F. L., von
770 Dobeneck, T., & Dekkers, M. J. (2007). Identification of magnetic Fe-Ti oxides in marine
771 sediments by electron backscatter diffraction in scanning electron microscopy. *Geophysical*
772 *Journal International*, *170*, 545–555.

Froelich, P. N., Klinkhammer, G. P., Bender, M. L., Luedtke, N. A., Heath, G. R., Cullen, D., Dauphin, P., Hammond, D., Hartman, B., & Maynard, V. (1979). Early oxidation of organic matter in pelagic sediments of the eastern equatorial Atlantic: Suboxic diagenesis. *Geochimica et Cosmochimica Acta*, *43*, 1075–1090.

Fu, Y., von Dobeneck, T., Franke, C., Heslop, D., & Kasten, S. (2008). Rock magnetic identification and geochemical process models of greigite formation in Quaternary marine sediments from the Gulf of Mexico (IODP Hole U1319A). *Earth and Planetary Science Letters*, *275*, 233–245.

Garming, J. F. L., Bleil, U., & Riedinger, N. (2005). Alteration of magnetic mineralogy at the sulfate–methane transition: Analysis of sediments from the Argentine continental slope. *Physics of the Earth and Planetary Interiors*, *151*, 290–308.

Garming, J. F. L., von Dobeneck, T., Franke, C., & Bleil, U. (2007). Low-temperature partial magnetic self-reversal in marine sediments by magnetostatic interaction of titanomagnetite and titanohematite intergrowths. *Geophysical Journal International*, *170*, 1067–1075.

Harrison, R. J., & Feinberg, J. M. (2008). FORCinel: An improved algorithm for calculating first-order reversal curve distributions using locally weighted regression smoothing. *Geochemistry, Geophysics, Geosystems*, *9*, Q05016, doi:10.1029/2008GC001987.

Harrison, R. J., & Lascu, I. (2014). FORCulator: A micromagnetic tool for simulating first-order reversal curve diagrams. *Geochemistry, Geophysics, Geosystems*, *15*, 4671–4691.

Harrison, R. J., Muraszko, J., Heslop, D., Lascu, I., Muxworthy, A. R., & Roberts, A. P. (2018). An improved algorithm for unmixing first-order reversal curve diagrams using principal component analysis, *Geochemistry, Geophysics, Geosystems*, *19*, https://doi.org/10.1029/2018GC007511.

Heslop, D. (2015). Numerical strategies for magnetic mineral unmixing, *Earth-Science Reviews*, *150*, 256–284.

798 Heslop, D., & Dillon, M. (2007). Unmixing magnetic remanence curves without *a priori*
799 knowledge. *Geophysical Journal International*, *170*, 556–566.
800 Heslop, D., Roberts, A. P., & Chang, L., 2014. Characterizing magnetofossils from first-order
801 reversal curve (FORC) central ridge signatures. *Geochemistry, Geophysics, Geosystems*, *15*,
802 2170–2179.
803 Heslop, D., Dekkers, M. J., Kruiver, P. P., & van Oorschot, I. H. M. (2002). Analysis of
804 isothermal remanent magnetization acquisition curves using the expectation-maximization
805 algorithm. *Geophysical Journal International*, *148*, 58–64.
806 Horng, C. S. (2018). Unusual magnetic properties of sedimentary pyrrhotite in methane seepage
807 sediments: Comparison with metamorphic pyrrhotite and sedimentary greigite. *Journal of*
808 *Geophysical Research: Solid Earth*, *123*, https://doi.org./10.1002/2017JB015262.
809 Horng, C. S., & Chen, K. H. (2006). Complicated magnetic mineral assemblages in marine
810 sediments offshore southwestern Taiwan: Possible influences of methane flux on the early
811 diagenetic processes. *Terrestrial, Atmospheric and Oceanic Sciences*, *17*, 1009–1026.
812 Horng, C. S., & Roberts, A. P. (2018). The low-temperature Besnus magnetic transition: Signals
813 due to monoclinic and hexagonal pyrrhotite. *Geochemistry, Geophysics, Geosystems*, *19*,
814 https://doi.org./10.1002/2017GC007394
815 Hounslow, M. W. (1996). Ferrimagnetic Cr and Mn spinels in sediments: Residual magnetic
816 minerals after diagenetic dissolution. *Geophysical Research Letters*, *23*, 2823–2826.
817 Housen, B. A., & Musgrave, R. J. (1996). Rock-magnetic signature of gas hydrates in accretionary
818 prism sediments. *Earth and Planetary Science Letters*, *139*, 509–519.
819 Jørgensen, B. B., & Kasten, S. (2006). Sulfur cycling and methane oxidation. In Schulz, H. D., &
820 Zabel, M. (Eds.), *Marine Geochemistry*, pp. 271–309.

Jørgensen, B. B., Böttcher, M. E., Lüschen, H., Neretin, L. N., & Volkov, I. I. (2004). Anaerobic methane oxidation and a deep H_2S sink generate isotopically heavy sulfides in Black Sea sediments. *Geochimica et Cosmochimica Acta*, *68*, 2095–2118.

Karlin, R. (1990a). Magnetite diagenesis in marine sediments from the Oregon continental margin. *Journal of Geophysical Research: Solid Earth*, *95*, 4405–4419.

Karlin, R. (1990b). Magnetic mineral diagenesis in suboxic sediments at Bettis site W-N, NE Pacific Ocean. *Journal of Geophysical Research: Solid Earth*, *95*, 4421–4436.

Karlin, R., & Levi, S. (1983). Diagenesis of magnetic minerals in Recent haemipelagic sediments. *Nature*, *303*, 327–330.

Karlin, R., & Levi, S. (1985). Geochemical and sedimentological control of the magnetic properties of hemipelagic sediments. *Journal of Geophysical Research: Solid Earth*, *90*, 10,373–10,392.

Kars, M., & Kodama, K. (2015a). Authigenesis of magnetic minerals in gas hydrate-bearing sediments in the Nankai Trough, offshore Japan. *Geochemistry, Geophysics, Geosystems*, *16*, 947–961.

Kars, M., & Kodama, K. (2015b). Rock magnetic characterization of ferrimagnetic iron sulfides in gas hydrate-bearing marine sediments at Site C0008, Nankai Trough, Pacific Ocean, off-coast Japan. *Earth, Planets and Space*, *67*, 118, doi:10.1186/s40623-015-0287-y.

Kasama, T., Pósfai, M., Chong, R. K. K., Finlayson, A. P., Buseck, P. R., Frankel, R. B., & Dunin-Borkowski, R. E. (2006). Magnetic properties, microstructure, composition, and morphology of greigite nanocrystals in magnetotactic bacteria from electron holography and tomography. *American Mineralogist*, *91*, 1216–1229.

Kasten, S., & Jørgensen, B. B. (2000). Sulfate reduction in marine sediments. In: Schulz, H. D., & Zabel, M. (Eds.), *Marine Geochemistry*, pp. 263–281.

Kasten, S., Freudenthal, T., Gingele, F. X., & Schulz, H. D. (1998). Simultaneous formation of iron-rich layers at different redox boundaries in sediments of the Amazon deep-sea fan. *Geochimica et Cosmochimica Acta*, *62*, 2253–2264.

Kawamura, N., Oda, H., Ikehara, K., Yamazaki, T., Shioi, K., Taga, S., Hatakeyama, S., & Torii, M. (2007). Diagenetic effect on magnetic properties of marine core sediments from the southern Okhotsk Sea. *Earth, Planets and Space*, *59*, 83–93.

Korff, L., von Dobeneck, T., Frederichs, T., Kasten, S., Kuhn, G., Gersonde, R., & Diekmann, B. (2016). Cyclic magnetite dissolution in Pleistocene sediments of the abyssal northwest Pacific Ocean: Evidence for glacial oxygen depletion and carbon trapping. *Paleoceanography*, *31*, 600–624.

Kruiver, P. P., Dekkers, M. J., & Heslop, D. (2001). Quantification of magnetic coercivity components by the analysis of acquisition curves of isothermal remanent magnetization. *Earth and Planetary Science Letters*, *189*, 269–276.

Lagroix, F., & Guyodo, Y. (2017). A new tool for separating the magnetic mineralogy of complex mineral assemblages from low temperature magnetic behavior. *Frontiers in Earth Science*, *5*, 61, doi: 10.3389/feart.2017.00061.

Larrasoaña, J. C., Roberts, A. P., Musgrave, R. J., Gràcia, E., Piñero, E., Vega, M., & Martínez-Ruiz, F. (2007). Diagenetic formation of greigite and pyrrhotite in marine sedimentary systems containing gas hydrates. *Earth and Planetary Science Letters*, *261*, 350–366.

Lascu, I., Harrison, R. J., Li, Y. T., Muraszko, J. R., Channell, J. E. T., Piotrowski, A. M., & Hodell, D. A. (2015). Magnetic unmixing of first-order reversal curve diagrams using principal component analysis. *Geochemistry, Geophysics, Geosystems*, *16*, 2900–2915.

Leslie, B. W., Lund, S. P., & Hammond, D. E. (1990a). Rock magnetic evidence for the dissolution and authigenic growth of magnetic minerals within anoxic marine sediments of the

869 California continental borderland. *Journal of Geophysical Research: Solid Earth, 95*, 4437–
870 4452.
871 Leslie, B. W., Hammond, D. E., Berelson, W. M., & Lund, S. P. (1990b). Diagenesis in anoxic
872 sediments from the California continental borderland and its influence on iron, sulfur, and
873 magnetite behavior. *Journal of Geophysical Research: Solid Earth, 95*, 4453–4470.
874 Levin, L. A. (2003). Oxygen minimum zone benthos: Adaptation and community response to
875 hypoxia. *Oceanography and Marine Biology: An Annual Review*, Gibson, R. N., & Atkinson,
876 R. J. A. (Eds.), *41*, 1–45.
877 Liu, J., Zhu, R. X., Roberts, A. P., Li, S. Q., & Chang, J. H. (2004). High-resolution analysis of
878 early diagenetic effects on magnetic minerals in post-middle-Holocene continental shelf
879 sediments from the Korea Strait. *Journal of Geophysical Research: Solid Earth*, *109*, B03103,
880 doi.10.1029/2003JB002813.
881 Liu, J. X., Liu, Q. S., Zhang, X. H., Liu, J., Wu, Z. Q., Mei, X., Shi, X. F., & Zhao, Q. H. (2016).
882 Magnetostratigraphy of a long Quaternary sediment core in the South Yellow Sea. *Quaternary*
883 *Science Reviews*, *144*, 1–15.
884 Mann, S., Sparks, N. H. C., Frankel, R. B., Bazylinski, D. A., & Jannasch, H. W. (1990).
885 Biomineralization of ferrimagnetic greigite (Fe_3S_4) and iron pyrite (FeS_2) in a magnetotactic
886 bacterium. *Nature*, *343*, 258–261.
887 Martín-Hernández, F., Dekkers, M. J., Bominaar-Silkens, I. M. A., & Maan, J. C. (2008).
888 Magnetic anisotropy behaviour of pyrrhotite as determined by low- and high-field experiments.
889 *Geophysical Journal International*, *174*, 42–54.
890 Mohamed, K. J., Rey, D., Rubio, B., Dekkers, M. J., Roberts, A. P., & Vilas, F. (2011). Onshore-
891 offshore gradient in reductive early diagenesis in coastal marine sediments of the Ria de Vigo,
892 Northwest Iberian Peninsula. *Continental Shelf Research*, *31*, 433–447.

893 Murray, J. W., Grundmanis, V., Smethie, J., & William, M. (1978). Interstitial water chemistry in
894 the sediments of Saanich Inlet. *Geochimica et Cosmochimica Acta*, *42*, 1011–1026.
895 Musgrave, R. J., Bangs, N. K., Larrasoaña, J. C., Gràcia, E., Hollamby, J. A., & Vega, M. E.
896 (2006). Rise of the base of the gas hydrate zone since the last glacial recorded by rock
897 magnetism. *Geology*, *34*, 117–120.
898 Muxworthy, A. R., & Dunlop, D. J. (2002). First-order reversal curve (FORC) diagrams for
899 pseudo-single-domain magnetites at high temperature. *Earth and Planetary Science Letters*,
900 *203*, 369–382.
901 Muxworthy, A. R., Heslop, D., & Williams, W. (2004). Influence of magnetostatic interactions on
902 first-order-reversal-curve (FORC) diagrams: A micromagnetic approach. *Geophysical*
903 *Journal International*, *158*, 888–897.
904 Muxworthy, A. R., King, J. G., & Heslop, D. (2005). Assessing the ability of first-order reversal
905 curve (FORC) diagrams to unravel complex magnetic signals. *Journal of Geophysical*
906 *Research: Solid Earth*, *110* (B1), doi:10.1029/2004JB003195.
907 Neretin, L. N., Böttcher, M. E., Jørgensen, B. B., Volkov, I. I., Lüschen, H., & Hilgenfeldt, K.
908 (2004). Pyritization processes and greigite formation in the advancing sulfidization front in
909 the Upper Pleistocene sediments of the Black Sea. *Geochimica et Cosmochimica Acta*, *68*,
910 2081–2093.
911 Newell, A. J. (2005). A high-precision model of first-order reversal curve (FORC) functions for
912 single-domain ferromagnets with uniaxial anisotropy. *Geochemistry, Geophysics,*
913 *Geosystems*, *6*, Q05010, doi:10.1029/2004GC000877.
914 Niewöhner, C., Hensen, C., Kasten, S., Zabel, M., & Schulz, H. D. (1998). Deep sulfate reduction
915 completely mediated by anaerobic methane oxidation in sediments of the upwelling area off
916 Namibia. *Geochimica et Cosmochimica Acta*, *62*, 455–464.

Oremland, R. S., & Taylor, B. F. (1978). Sulfate reduction and methanogenesis in marine sediments. *Geochimica et Cosmochimica Acta*, *42*, 209–214.

Ouyang, T., Heslop, D., Roberts, A. P., Tian, C., Zhu, Z., Qiu, Y., & Peng, X. (2014). Variable remanence acquisition efficiency in sediments containing biogenic and detrital magnetites: Implications for relative paleointensity signal recording. *Geochemistry, Geophysics, Geosystems*, *15*, 2780–2796.

Pike, C., and A. Fernandez (1999), An investigation of magnetic reversal in submicron-scale Co dots using first order reversal curve diagrams, *J. Appl. Phys.*, *85*, 6668–6676.

Pike, C. R., Roberts, A. P., & Verosub, K. L. (1999). Characterizing interactions in fine magnetic particle systems using first order reversal curves. *Journal of Applied Physics*, *85*, 6660–6667.

Pike, C. R., Roberts, A. P., & Verosub, K. L. (2001a). First-order reversal curve diagrams and thermal relaxation effects in magnetic particles. *Geophysical Journal International*, *145*, 721–730.

Pike, C. R., Roberts, A. P., Dekkers, M. J., & Verosub, K. L. (2001b). An investigation of multi-domain hysteresis mechanisms using FORC diagrams. *Physics of the Earth and Planetary Interiors*, *126*, 11–25.

Pósfai, M., Buseck, P. R., Bazylinski, D. A., & Frankel, R. B. (1998a). Iron sulfides from magnetotactic bacteria: Structure, composition, and phase transitions. *American Mineralogist*, *83*, 1469–1481.

Pósfai, M., Buseck, P. R., Bazylinski, D. A., & Frankel, R. B. (1998b). Reaction sequence of iron sulfide minerals in bacteria and their use as biomarkers. *Science*, *280*, 880–883.

Reinholdsson, M., Snowball, I., Zillén, L., Lenz, C., & Conley, D. J. (2013). Magnetic enhancement of Baltic Sea sapropels by greigite magnetofossils. *Earth and Planetary Science Letters*, *366*, 137–150.

941 Rey, D., Mohamed, K. J., Bernabeu, A., Rubio, B., & Vilas, F. (2005). Early diagenesis of
942 magnetic minerals in marine transitional environments: Geochemical signatures of
943 hydrodynamic forcing. *Marine Geology*, *215*, 215–236.
944 Richter, C., Hayashida, A., Guyodo, Y., Valet, J. P., & Verosub, K. L. (1999). Magnetic intensity
945 loss and core diagenesis in long-core samples from the East Cortez Basin and the San Nicolas
946 Basin (California Borderland). *Earth, Planets and Space*, *51*, 329–336.
947 Riedinger, N., Pfeifer, K., Kasten, S., Garming, L. F. L., Vogt, C., & Hensen, C. (2005).
948 Diagenetic alteration of magnetic signals by anaerobic oxidation of methane related to a
949 change in sedimentation rate. *Geochimica et Cosmochimica Acta*, *69*, 4117–4126.
950 Riedinger, N., Formolo, M. J., Lyons, T. W., Henkel, S., Beck, A., & Kasten, S. (2014). An
951 inorganic geochemical argument for coupled anaerobic oxidation of methane and iron
952 reduction in marine sediments. *Geobiology*, *12*, 172–181.
953 Roberts, A. P. (1995). Magnetic characteristics of sedimentary greigite (Fe_3S_4). *Earth and*
954 *Planetary Science Letters*, *134*, 227–236.
955 Roberts, A. P. (2015). Magnetic mineral diagenesis. *Earth-Science Rev*iews, *151*, 1–47.
956 Roberts, A. P., & Turner, G. M. (1993). Diagenetic formation of ferrimagnetic iron sulphide
957 minerals in rapidly deposited marine sediments, South Island, New Zealand. *Earth and*
958 *Planetary Science Letters*, *115*, 257–273.
959 Roberts, A. P., & Weaver, R. (2005). Multiple mechanisms of remagnetization involving
960 sedimentary greigite (Fe_3S_4). *Earth and Planetary Science Letters*, *231*, 263–277.
961 Roberts, A. P., Pike, C. R., & Verosub, K. L. (2000). First-order reversal curve diagrams: A new
962 tool for characterizing the magnetic properties of natural samples. *Journal of Geophysical*
963 *Research: Solid Earth*, *105*, 28,461–28,475.
964 Roberts, A. P., Jiang, W. T., Florindo, F., Horng, C. S., & Laj, C. (2005). Assessing the timing of
965 greigite formation and the reliability of the Upper Olduvai polarity transition record from the

966 Crostolo River, Italy. *Geophysical Research Letters*, *32*, L05307,
967 doi:10.1029/2004GL022137.
968 Roberts, A. P., Liu, Q. S., Rowan, C. J., Chang, L., Carvallo, C., Torrent, J., & Horng, C. S.
969 (2006). Characterization of hematite (α-Fe_2O_3), goethite (α-FeOOH), greigite (Fe_3S_4), and
970 pyrrhotite (Fe_7S_8) using first-order reversal curve diagrams. *Journal of Geophysical Research:*
971 *Solid Earth*, *111*, B12S35, doi:10.1029/2006JB004715.
972 Roberts, A. P., Florindo, F., Larrasoaña, J. C., O'Regan, M. A., & Zhao, X. (2010). Complex
973 polarity pattern at the (former) Plio-Pleistocene global stratotype section at Vrica (Italy):
974 Remagnetization by magnetic iron sulphides. *Earth and Planetary Science Letters*, *292*, 98–
975 111.
976 Roberts, A. P., Chang, L., Rowan, C. J., Horng, C. S., & Florindo, F. (2011). Magnetic
977 characteristics of sedimentary greigite (Fe_3S_4): An update. *Reviews of Geophysics*, *49*,
978 RG1002, doi:10.1029/2010RG000336.
979 Roberts, A. P., Chang, L., Heslop, D., Florindo, F., & Larrasoaña, J. C. (2012). Searching for
980 single domain magnetite in the 'pseudo-single-domain' sedimentary haystack: Implications of
981 biogenic magnetite preservation for sediment magnetism and relative paleointensity
982 determinations. *Journal of Geophysical Research: Solid Earth*, *117*, B08104,
983 doi:10.1029/2012JB009412.
984 Roberts, A. P., Florindo, F., Chang, L., Heslop, D., Jovane, L., & Larrasoaña, J. C. (2013).
985 Magnetic properties of pelagic marine carbonates. *Earth-Science Reviews*, *127*, 111–139.
986 Roberts, A. P., Heslop, D., Zhao, X., & Pike, C. R. (2014). Understanding fine magnetic particle
987 systems through use of first-order reversal curve diagrams. *Reviews of Geophysics*, *52*, 557–
988 602.

989 Roberts, A. P., Almeida, T. P., Church, N. S., Harrison, R. J., Heslop, D., Li, Y. L., Li, J. H.,
990 Muxworthy, A. R., Williams, W., & Zhao, X. (2017). Resolving the origin of pseudo-single
991 domain magnetic behavior. *Journal of Geophysical Research: Solid Earth*, *122*, 9534–9558.
992 Robertson, D. J., & France, D. E. (1994). Discrimination of remanence-carrying minerals in
993 mixtures, using isothermal remanent magnetisation acquisition curves. *Physics of the Earth and*
994 *Planetary Interiors*, *84*, 223–234.
995 Robinson, S. G., Sahota, J. T. S., & Oldfield, F. (2000). Early diagenesis in North Atlantic abyssal
996 plain sediments characterized by rock-magnetic and geochemical indices. *Marine Geology*,
997 *163*, 77–107.
998 Rochette, P., Mathé, P. E., Esteban, L., Rakoto, H., Bouchez, J. L., Liu, Q. S., & Torrent, J.
999 (2005). Non-saturation of the defect moment of goethite and fine-grained hematite up to 57
1000 Teslas. *Geophysical Research Letters*, *32*, L22309, doi:10.1029/2005GL024196.
1001 Rowan, C. J., & Roberts, A. P. (2006). Magnetite dissolution, diachronous greigite formation, and
1002 secondary magnetizations from pyrite oxidation: Unravelling complex magnetizations in
1003 Neogene marine sediments from New Zealand. *Earth and Planetary Science Letters*, *241*, 119–
1004 137.
1005 Rowan, C. J., & Roberts, A. P. (2008). Widespread remagnetizations and a new view of Neogene
1006 tectonic rotations within the Australia-Pacific plate boundary zone, New Zealand. *Journal of*
1007 *Geophysical Research: Solid Earth*, *113*, B03103, doi:10.1029/2006JB004594.
1008 Rowan, C. J., Roberts, A. P., & Broadbent, T. (2009). Reductive diagenesis, magnetite dissolution,
1009 greigite growth and paleomagnetic smoothing in marine sediments: A new view. *Earth and*
1010 *Planetary Science Letters*, *277*, 223–235.
1011 Rudmin, M., Roberts, A. P., Horng, C. S., Mazurov, A., Savinova, O., Ruban, A., Kashapov, R.,
1012 & Veklich, M. (2018). Ferrimagnetic iron sulfide formation and methane venting across the

Paleocene-Eocene Thermal Maximum in shallow marine sediments, ancient West Siberian Sea. *Geochemistry, Geophysics, Geosystems*, *19*, 21–42.

Segarra, K. E. A., Comerford, C., Slaughter, J., & Joye, S. B. (2013). Impact of electron acceptor availability on the anaerobic oxidation of methane in coastal freshwater and brackish wetland sediments. *Geochimica et Cosmochimica Acta*, *115*, 15–30.

Shi, M. N., Wu, H. C., Roberts, A. P., Zhang, S. H., Zhao, X. X., Li, H. Y., Su, X., Yang, T. S., Chang, L., Hu, P. X., Zhao, X., & Wang, H. Q. (2017). Tectonic, climatic, and diagenetic control of magnetic properties of sediments from Kumano Basin, Nankai margin, southwestern Japan. *Marine Geology*, *391*, 1–12.

Sivan, O., Adler, M., Pearson, A., Gelman, F., Bar-Or, I., & John, S. G. (2011). Geochemical evidence for iron-mediated anaerobic oxidation of methane. *Limnology and Oceanography*, *56*, 1536–1544.

Tric, E., Laj, C., Jehanno, C., Valet, J. P., Kissel, C., Mazaud, A., & Iaccarino, S. (1991). High-resolution record of the Upper Olduvai transition from Po Valley (Italy) sediments: Support for dipolar transition geometry? *Physics of the Earth and Planetary Interiors*, *65*, 319–336.

van Dongen, B. E., Roberts, A. P., Schouten, S., Jiang, W. T., Florindo, F., & Pancost, R. D. (2007). Formation of iron sulfide nodules during anaerobic oxidation of methane. *Geochimica et Cosmochimica Acta*, *71*, 5155–5167.

Vasiliev, I., Dekkers, M. J., Krijgsman, W., Franke, C., Langereis, C. G., & Mullender, T. A. T. (2007). Early diagenetic greigite as a recorder of the palaeomagnetic signal in Miocene-Pliocene sedimentary rocks of the Carpathian foredeep (Romania). *Geophysical Journal International*, *171*, 613–629.

Weaver, R., Roberts, A. P., & Barker, A. J. (2002). A late diagenetic (syn-folding) magnetization carried by pyrrhotite: Implications for paleomagnetic studies from magnetic iron sulphide-bearing sediments. *Earth and Planetary Science Letters*, *200*, 371–386.

Wehland, F., Stancu, A., Rochette, P., Dekkers, M. J., & Appel, E. (2005). Experimental evaluation of magnetic interaction in pyrrhotite bearing samples. *Physics of the Earth and Planetary Interiors*, *153*, 181–190.

Yamazaki, T. (2008). Magnetostatic interactions in deep-sea sediments inferred from first-order reversal curve diagrams: Implications for relative paleointensity normalization. *Geochemistry, Geophysics, Geosystems*, *9*, Q02005, doi:10.1029/2007GC001797.

Yamazaki, T. (2009). Environmental magnetism of Pleistocene sediments in the North Pacific and Ontong-Java Plateau: Temporal variations of detrital and biogenic components. *Geochemistry, Geophysics, Geosystems*, *10*, Q07Z04, doi:10.1029/2009GC002413.

Yamazaki, T., Abdeldayem, A. L., & Ikehara, K. (2003). Rock-magnetic changes with reduction diagenesis in Japan Sea sediments and preservation of geomagnetic secular variation in inclination during the last 30,000 years. *Earth, Planets and Space*, *55*, 327–340.

Zhao, X., Roberts, A. P., Heslop, D., Paterson, G. A., Li, Y. L., & Li, J. H. (2017). Magnetic domain state diagnosis using hysteresis reversal curves. *Journal of Geophysical Research: Solid Earth*, *122*, 4767–4789. doi:10.1002/2016jb013683.

Figure captions

Figure 1 Cartoon representation of the depth distribution of sedimentary redox-driven diagenetic zones. Electron acceptors and respiration processes by which reactants are consumed are indicated on the left. Idealized pore water profiles of reactants (O_2, NO_2^-, NO_3^-) and products (NO_3^-, Mn^{2+}, Fe^{2+}, H_2S, CH_4) and associated chemical zones are shown on the right (modified from Jørgensen and Kasten (2006), Canfield and Thamdrup (2009), and Roberts (2015)). The names used for chemical zones are from Canfield and Thamdrup (2009). Authigenic iron minerals that can form in the respective chemical zones are listed in the far right-hand column (modified from Berner, 1981).

Figure 2 Representative FORC diagrams for fine magnetic particle systems with different dominant domain states. Examples are individual samples discussed later in this study, except (f). (a) Non-interacting SD particles with part of the particle assemblage near the SP/SD threshold size (see Pike et al. (2001a) for details). Sample MH30 from New Zealand, with the following VARIFORC smoothing parameters (Egli, 2013): $s_{c,0}$ = 8, $s_{c,1}$ = 10, $s_{b,0}$ = 7, $s_{b,1}$ = 10, and $\lambda_c = \lambda_b = 0.2$. Such diagenetically reduced samples are usually weakly magnetized and noisy. (b) Strongly interacting stable SD particles (see Pike et al. (1999) and Roberts et al. (2000, 2014) for details). Sample WB26 from New Zealand, with the following VARIFORC smoothing parameters (Egli, 2013): $s_{c,0}$ = 5, $s_{c,1}$ = 7, $s_{b,0}$ = 4, $s_{b,1}$ = 7, and $\lambda_c = \lambda_b = 0.1$. (c) Moderately magnetostatically interacting stable SD particles with multi-axial anisotropy (see Harrison & Lascu (2014) for details). Sample SDC3950 from Italy, with the following VARIFORC smoothing parameters (Egli, 2013): $s_{c,0}$ = 5, $s_{c,1}$ = 8, $s_{b,0}$ = 5, $s_{b,1}$ = 8, and $\lambda_c = \lambda_b =$ 0.1. (d) SD/vortex state particles (see Pike and Fernandez (1999) and Roberts et al. (2017) for details). Sample CD1431056 from the Arabian Sea, with the following VARIFORC smoothing parameters (Egli, 2013): $s_{c,0}$ = 5, $s_{c,1}$ = 8, $s_{b,0}$ = 5, $s_{b,1}$ = 8, and $\lambda_c = \lambda_b = 0.1$. (e) MD particles typically seen in natural samples (Roberts et al., 2000; Pike et al., 2001b). Sample NR27 from

New Zealand, with the following VARIFORC smoothing parameters (Egli, 2013): $s_{c,0}$ = 5, $s_{c,1}$ = 7, $s_{b,0}$ = 4, $s_{b,1}$ = 7, and $\lambda_c = \lambda_b$ = 0.1. (f) MD particles seen in coarser systems dominated by domain wall pinning (see Pike et al. (2001b) and Roberts et al. (2014) for details). Geological samples rarely have such behaviour; the example is a silicon steel sample with conventional FORC smoothing with smoothing factor = 4.

Figure 3 FORC unmixing results for ferruginous to sulfidic diagenetic environments in core CD143-55705. Distribution of PCs for 50 measured FORC diagrams in (a) PC1-PC2 space, (b) PC1-PC3 space, and (c) PC2-PC3 space. Data for the lower part of the core (enclosed by an ellipse in (a)) are noisy and are treated separately (26 samples)). Data for the upper part of the core (enclosed by an ellipse in (a); 24 samples) define a triangular region in (b) from which three EMs are defined where (d) is a non-interacting stable SD/vortex state component (EM1) due to biogenic and detrital magnetite, (e) is a coarser vortex state to MD component (EM2) due to detrital magnetic minerals, and (f) is an authigenic SP-SD component (EM3) that formed during early diagenesis. Sets of FORCs shown for EMs in this and other figures are usually incomplete representations. For experimental measurements, a set of FORCs provides an outline of the major hysteresis loop and is approximately symmetrical, whereas the lower part of the set of FORCs for EMs is usually not shown because the lowermost FORCs represent areas that lie outside the limits defined for the EM FORC diagrams. In such a representation, EM FORCs will, thus, usually appear truncated and asymmetrical, and can possibly appear distorted. The triangular mixing space with positions of the three EMs is shown in (g), where contours indicate the space where FORC distributions start to become physically unrealistic (see Harrison et al. (submitted ms)). The arrow indicates the general down-core trend from EM1 to EM2 to EM3. (h) Representation of the noisy data from the lower part of the core (ellipse in (a)) that were averaged to obtain (i) a FORC diagram defined where PC1 and PC2 equal zero in (h). (j) Down-core IRM profile (gray) with relative contributions of EM1, EM2,

and EM3. VARIFORC parameters (see Egli (2013)) for smoothing of the PCA solution are: $s_{c,0}$ = 5, $s_{c,1}$ = 8, $s_{b,0}$ = 5, $s_{b,1}$ = 8, and $\lambda_c = \lambda_b = 0.1$. The maximum applied field for FORC measurements was 500 mT, which is sufficient to saturate magnetically the low-coercivity minerals in the studied samples.

Figure 4 FORC unmixing results for ferruginous to sulfidic diagenetic environments in marine sediment core LC13-81-G138. Distribution of PCs for 15 measured FORC diagrams in (a) PC1-PC2 space, (b) PC1-PC3 space, and (c) PC2-PC3 space for core LC13-81-G138. Data for the lower part of the core (scattered data to the left in (a) and (b)) are noisy and are treated separately (10 samples)). Data for the upper part of the core (enclosed by an ellipse in (b); 5 samples) define a binary mixing line from which 2 EMs are defined where (d) is a non-interacting stable SD component (EM1) due to biogenic magnetite and (e) is a coarser vortex state component (EM2) due to detrital magnetic minerals. (f) An authigenic SP-SD component (EM3) that formed during early diagenesis is obtained by averaging the noisy FORC data indicated in (h) where PC1 and PC2 equal zero. (g) Binary mixing space with positions of 2 EMs for the upper part of the core. (i) Down-core IRM profile (gray) with relative contributions of EM1 and EM2 for the upper part of the core. VARIFORC parameters (see Egli (2013)) for smoothing of the PCA solution are: $s_{c,0}$ = 5, $s_{c,1}$ = 8, $s_{b,0}$ = 5, $s_{b,1}$ = 8, and $\lambda_c = \lambda_b = 0.1$. The maximum applied field for FORC measurements was 500 mT, which is sufficient to saturate magnetically the low-coercivity minerals in the studied samples.

Figure 5 FORC unmixing results for sulfidic diagenetic environments in Middle Pleistocene Italian fluvial clays (Florindo et al., 2007). (a) EM1 is magnetostatically interacting stable SD greigite, where the negative region at –45° is indicative of multi-axial anisotropy (see Harrison & Lascu (2014)). (b) EM2 is a magnetostatically interacting stable SD greigite component with higher coercivity than EM1. (c) EM3 is an authigenic SP-SD component that is observed in all environments analysed here (defined by the average for 4 weakly magnetized samples). (d) The

triangular mixing space with positions of the three EMs for 16 samples, where the contours indicate the space where FORC distributions start to become physically unrealistic. (e-h) FORC diagrams for measured samples, which fall dominantly near (g, h) EM2, with mixtures with (e) EM3 and (f) EM1. VARIFORC parameters (see Egli (2013)) for smoothing of the PCA solution are: $s_{c,0}$ = 8, $s_{c,1}$ = 10, $s_{b,0}$ = 7, $s_{b,1}$ = 10, and $\lambda_c = \lambda_b$ = 0.1. The maximum applied field for FORC measurements was 500 mT, which is sufficient to saturate magnetically the low-coercivity minerals in the studied samples.

Figure 6 FORC unmixing results for sulfidic (and methanic) diagenetic environments in tectonically uplifted Lower Pleistocene marine mudstones from Crostolo River, Italy (Roberts et al., 2005). (a) EM1 represents magnetostatically interacting pyrrhotite, where the negative region at –45° is indicative of multi-axial anisotropy (see Harrison & Lascu (2014)). (b) EM2 is a magnetostatically interacting stable SD greigite component. (c) EM3 is an authigenic SP-SD component that is observed in all environments analysed here. (d, e) Triangular PC1-PC2 mixing space (12 samples) with (d) 4 scattered weakly magnetized samples from which 3 EMs are defined and (e) all samples, where the dominant behavior is scattered around EM2. Contours in (d, e) indicate the space where FORC distributions start to become physically unrealistic. (f-i) FORC diagrams for measured samples, which range from (f) being dominated by EM2, (g) near EM1, (h) mixture of EM1 and EM3, and (i) mixture of EM2 and EM3. VARIFORC parameters (see Egli (2013)) for smoothing of the PCA solution are: $s_{c,0}$ = 8, $s_{c,1}$ = 10, $s_{b,0}$ = 7, $s_{b,1}$ = 10, and $\lambda_c = \lambda_b$ = 0.1. The maximum applied field for FORC measurements was 500 mT, which is sufficient to saturate magnetically the low-coercivity minerals in the studied samples.

Figure 7 FORC unmixing results for sulfidic diagenetic environments in tectonically uplifted Neogene marine sediments from eastern New Zealand (Rowan and Roberts, 2006). Four EMs are identified, where (a) EM1 is a coarse detrital iron oxide component, and (b) EM2

is stable SD greigite with strong magnetostatic interactions. EM3 and EM4 link the other two components, where both have a strong SP signal, but (c) EM3 contains a SD/vortex state detrital fraction, and (d) EM4 comprises a less strongly interacting SP/SD greigite component. (e, f) Visualizations of a tetrahedral mixing space (129 samples) for: (e) PC1-PC2 and (f) PC1-PC3. (g-j) Representative FORC diagrams for measured samples that represent mixtures between (g) EM1 and EM3, (h) EM1, EM3, and EM4, (i) EM2, EM3, and EM4, and (j) EM2, EM3, and EM4. VARIFORC parameters (see Egli (2013)) for smoothing of the PCA solution are: $s_{c,0}$ = 8, $s_{c,1}$ = 10, $s_{b,0}$ = 7, $s_{b,1}$ = 10, and $\lambda_c = \lambda_b$ = 0.1. The maximum applied fields for FORC measurements were either 500 or 1000 mT, which is sufficient to saturate magnetically the low-coercivity minerals in the studied samples.

Figure 8 FORC unmixing results for sulfidic and methanic diagenetic environments in sediments with active methane venting from Hydrate Ridge, Cascadia margin, offshore of Oregon, USA (Larrasoaña et al., 2007). Four EMs are identified, where (a) EM1 is a coarse detrital iron oxide component (in turbidite samples), (b) EM2 is stable SD greigite with strong magnetostatic interactions, (c) EM3 is an authigenic SP-SD component, and (d) EM4 is magnetostatically interacting pyrrhotite, where the negative region at –45° is indicative of multi-axial anisotropy (see Harrison & Lascu (2014)). (e, f) Visualizations of tetrahedral mixing (20 samples) for: (e) PC1-PC2 and (f) PC1-PC3. (g, h) Representative FORC diagrams for measured samples that represent mixtures between (g) EM2 and EM4, and (h) EM2 and EM3. The mixing space is well defined by measured samples that represent each EM, so contours are not shown to indicate the space for physically realistic FORCs. VARIFORC parameters (see Egli (2013)) for smoothing of the PCA solution are: $s_{c,0}$ = 5, $s_{c,1}$ = 7, $s_{b,0}$ = 4, $s_{b,1}$ = 7, and $\lambda_c = \lambda_b$ = 0.1. The maximum applied field for FORC measurements was 500 mT, which is sufficient to saturate magnetically the low-coercivity minerals in the studied samples.

Figure 9 Illustration of typical FORC diagrams encountered in different diagenetic environments. (a) Schematic pore water profile for progressive steady state diagenesis and (b) chemical zones from Figure 1. FORC diagrams that are typical of (c) biogenic magnetite and (d) biogenic magnetite and a fine detrital magnetite fraction are encountered typically in oxic to ferruginous environments. Biogenic magnetite ceases to be stable in ferruginous environments. Variable FORC diagrams are typically observed for detrital magnetic mineral assemblages containing magnetite with variable grain sizes as illustrated in (e-g), where coarse magnetite remains stable in oxic to manganous zones and starts to dissolve in the ferruginous zone. Iron oxides are unstable in the sulfidic and methanic zones and are unlikely to survive (unless they occur as inclusions within silicate particles; e.g., Chang et al. (2016b, c)). At the SMT, dissolved sulfide reacts with any available Fe^{2+} to form (h) SP/SD greigite. If Fe^{2+} is available in the methanic zone, stable SD authigenic pyrrhotite can grow (i). Stable SD greigite (j) is encountered widely in reducing diagenetic environments, but it has not been linked definitively to the SMT and it could form deeper within the sediment column where Fe^{2+} is available and AOM creates a source of H_2S to enable greigite formation. The location of stable SD greigite formation is, therefore, indicated with question marks. Note that while the FORC diagrams presented in this figure are typical of the environments in question they are not necessarily unique to these environments.

Figure 1.

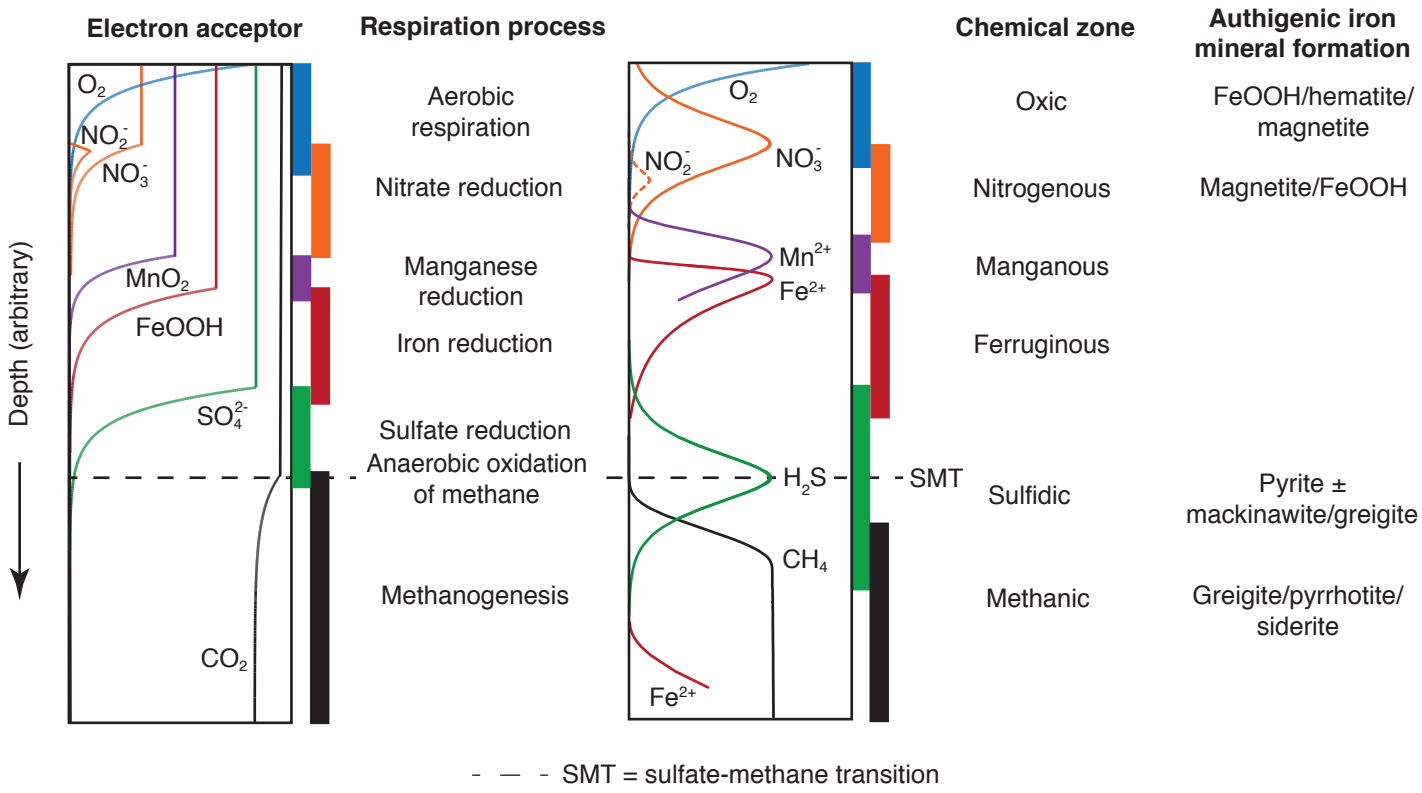
Electron acceptor
Respiration process
Chemical zone
Authigenic iron mineral formation
Depth (arbitrary)
O2
NO2-
NO3-
MnO2
FeOOH
SO4 2-
CO2
Aerobic respiration
Nitrate reduction
Manganese reduction
Iron reduction
Sulfate reduction
Anaerobic oxidation of methane
Methanogenesis
Oxic
Nitrogenous
Manganous
Ferruginous
Sulfidic
Methanic
FeOOH/hematite/ magnetite
Magnetite/FeOOH
Pyrite ± mackinawite/greigite
Greigite/pyrrhotite/ siderite
Mn2+
Fe2+
H2S
SMT
CH4
- — - SMT = sulfate-methane transition

Figure 2.

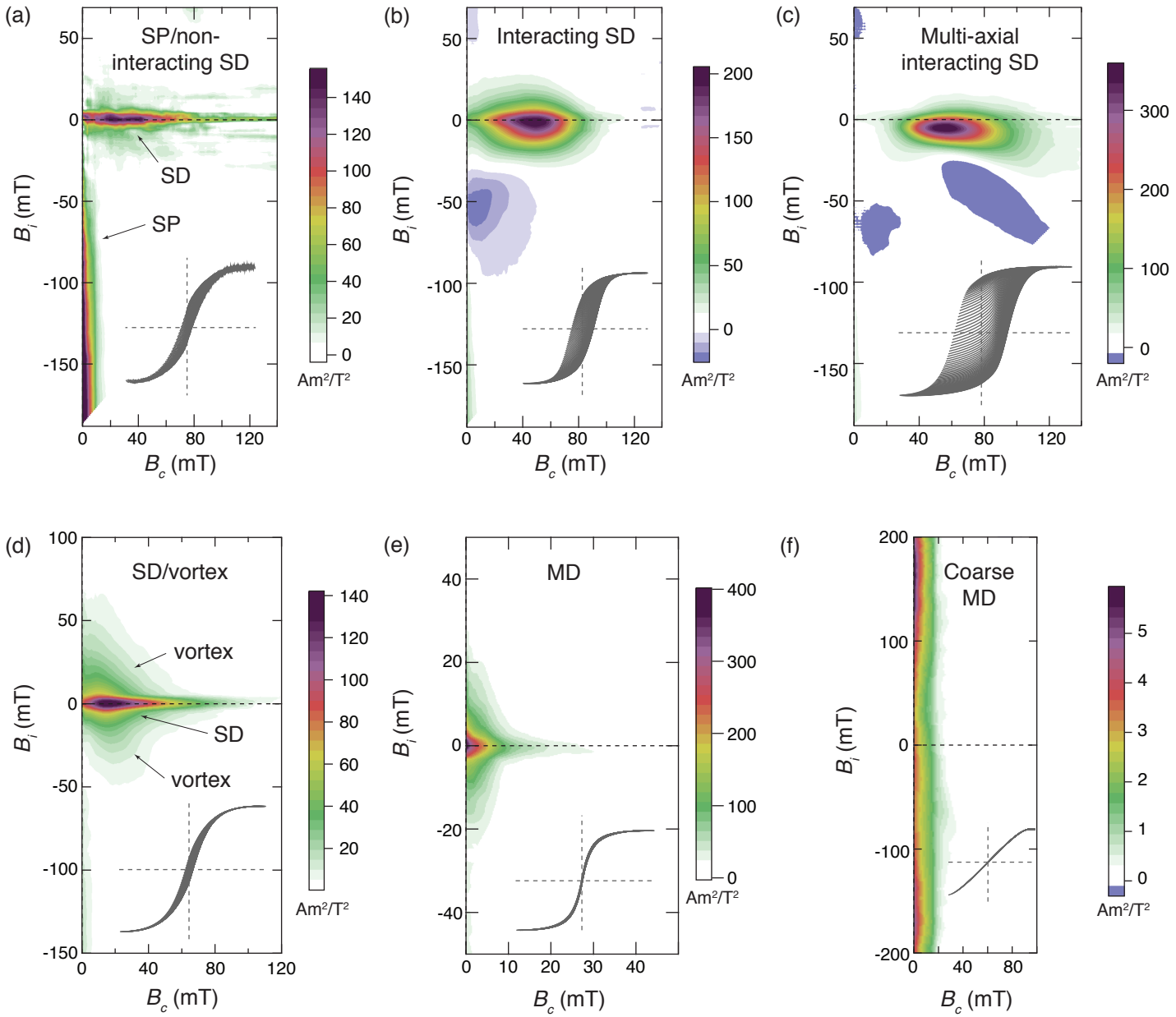
(a)
SP/non-interacting SD
SD
SP
(b)
Interacting SD
(c)
Multi-axial interacting SD
(d)
SD/vortex
vortex
SD
vortex
(e)
MD
(f)
Coarse MD
B_i (mT)
B_c (mT)
Am²/T²

Figure 3.

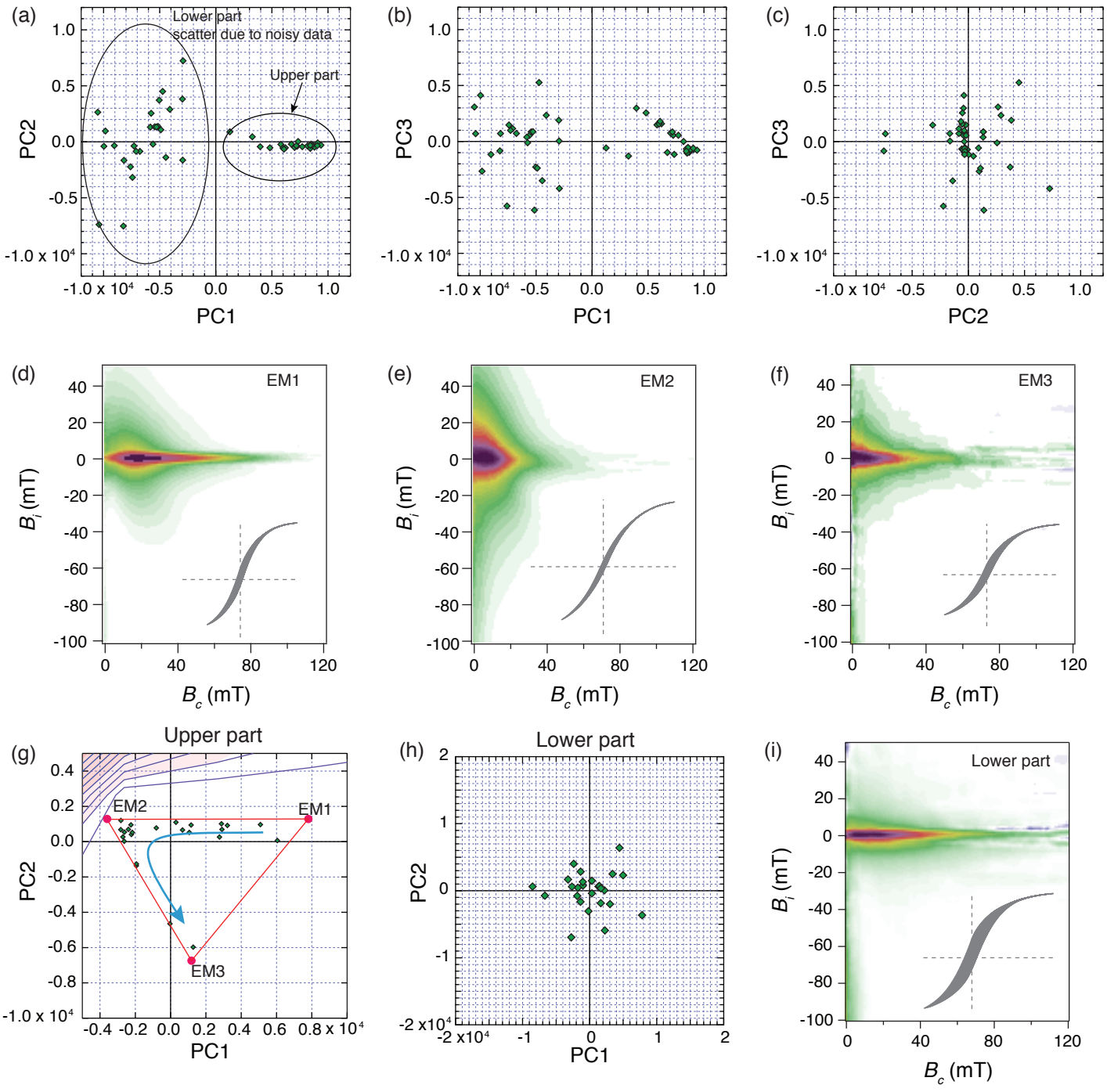
(a)
Lower part
scatter due to noisy data
Upper part
PC2
PC1
(b)
PC3
PC1
(c)
PC3
PC2
(d)
EM1
B_i (mT)
B_c (mT)
(e)
EM2
B_i (mT)
B_c (mT)
(f)
EM3
B_i (mT)
B_c (mT)
(g)
Upper part
EM2
EM1
EM3
PC2
PC1
(h)
Lower part
PC2
PC1
(i)
Lower part
B_i (mT)
B_c (mT)
(j)
IRM
EM1
EM2
EM3
IRM (Am²)
Relative contribution of EMs
Depth (m)

Figure 4.

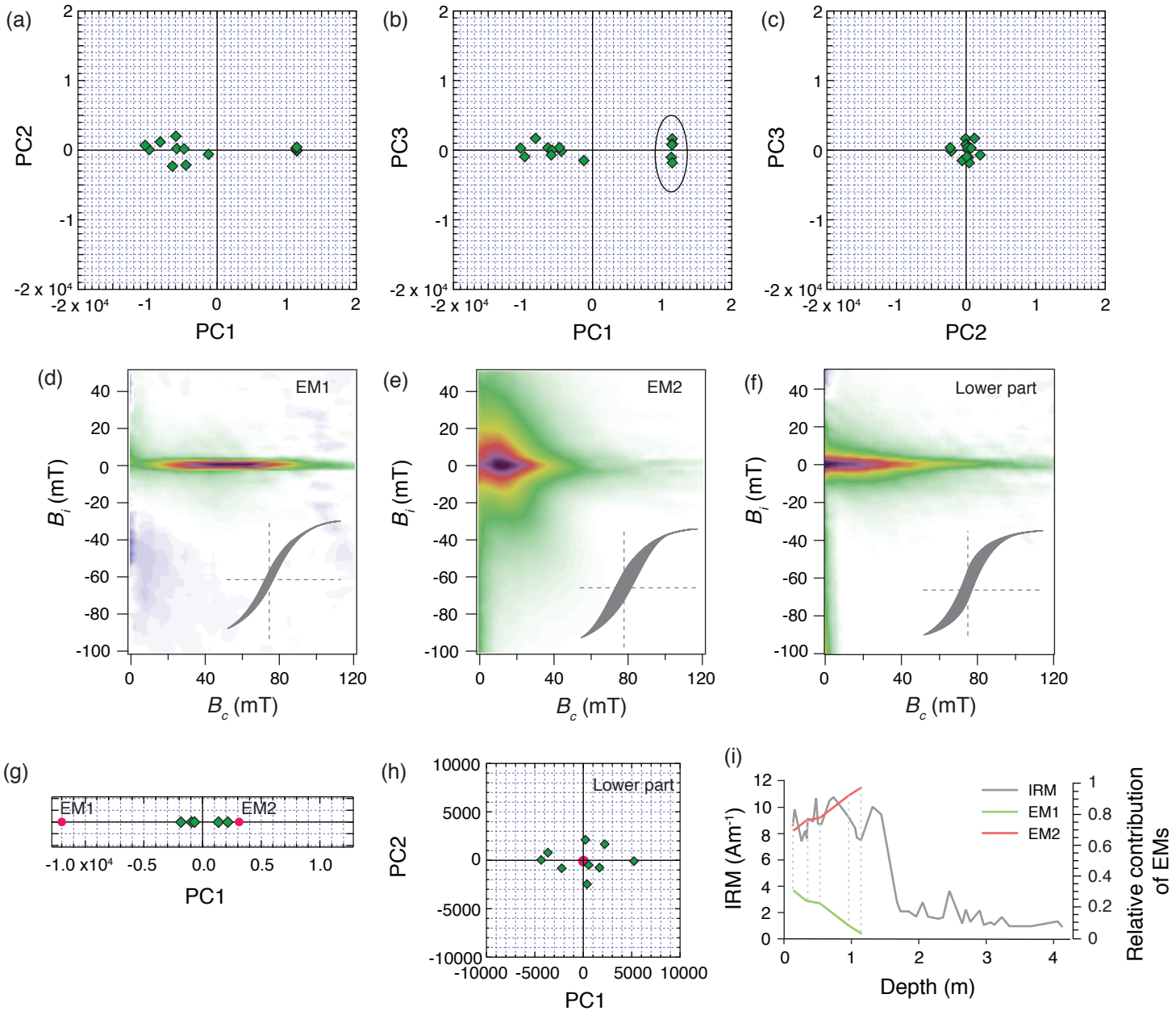
(a)
PC2
PC1
(b)
PC3
PC1
(c)
PC3
PC2
(d)
EM1
B_i (mT)
B_c (mT)
(e)
EM2
B_i (mT)
B_c (mT)
(f)
Lower part
B_i (mT)
B_c (mT)
(g)
EM1
EM2
PC1
(h)
Lower part
PC2
PC1
(i)
IRM
EM1
EM2
IRM (Am^{-1})
Depth (m)
Relative contribution of EMs

Figure 5.

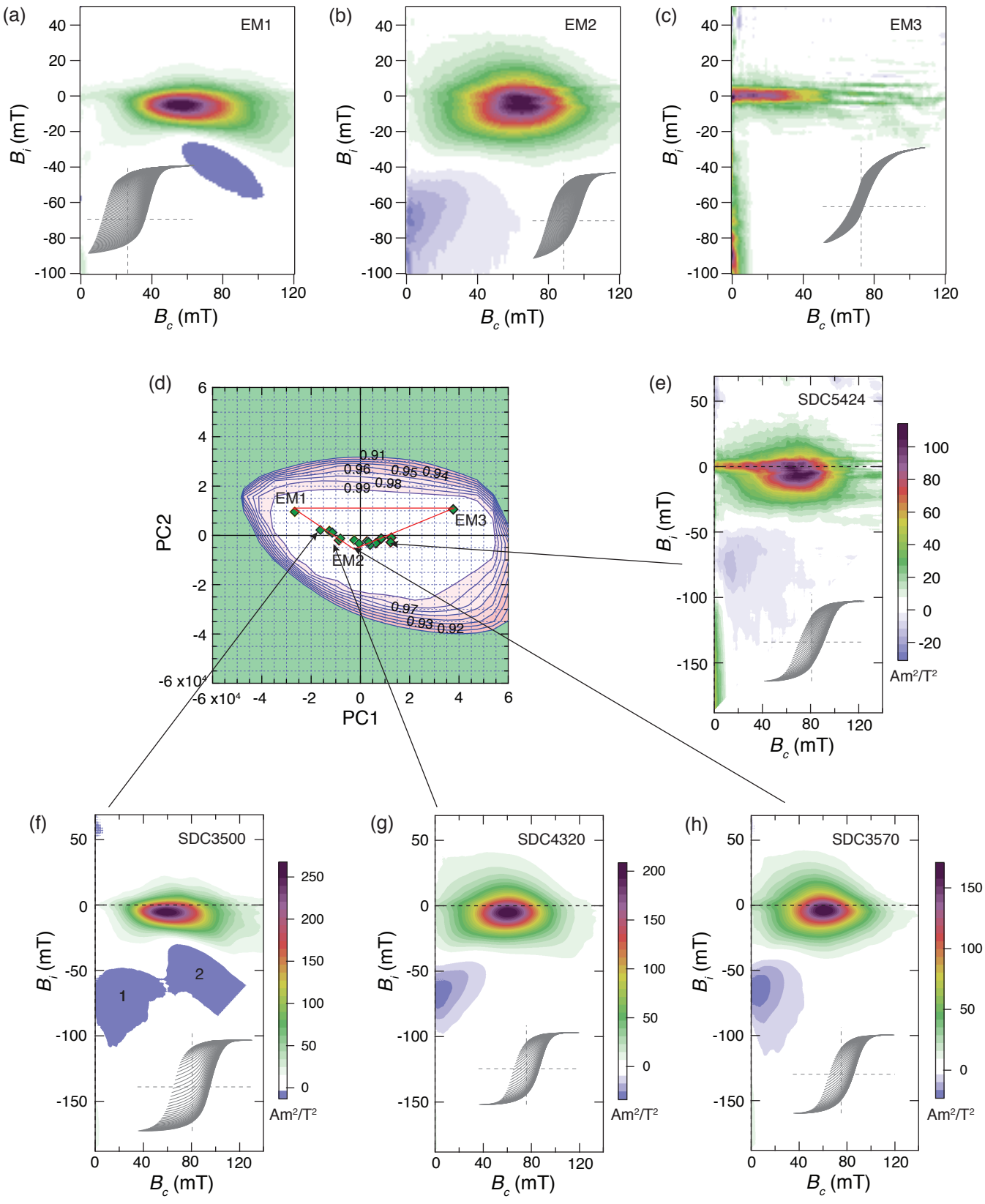
(a)
EM1
(b)
EM2
(c)
EM3
B_i (mT)
B_c (mT)
(d)
PC1
PC2
EM1
EM2
EM3
0.91
0.96
0.95
0.94
0.99
0.98
0.97
0.93
0.92
(e)
SDC5424
(f)
SDC3500
1
2
(g)
SDC4320
(h)
SDC3570
Am²/T²

Figure 6.

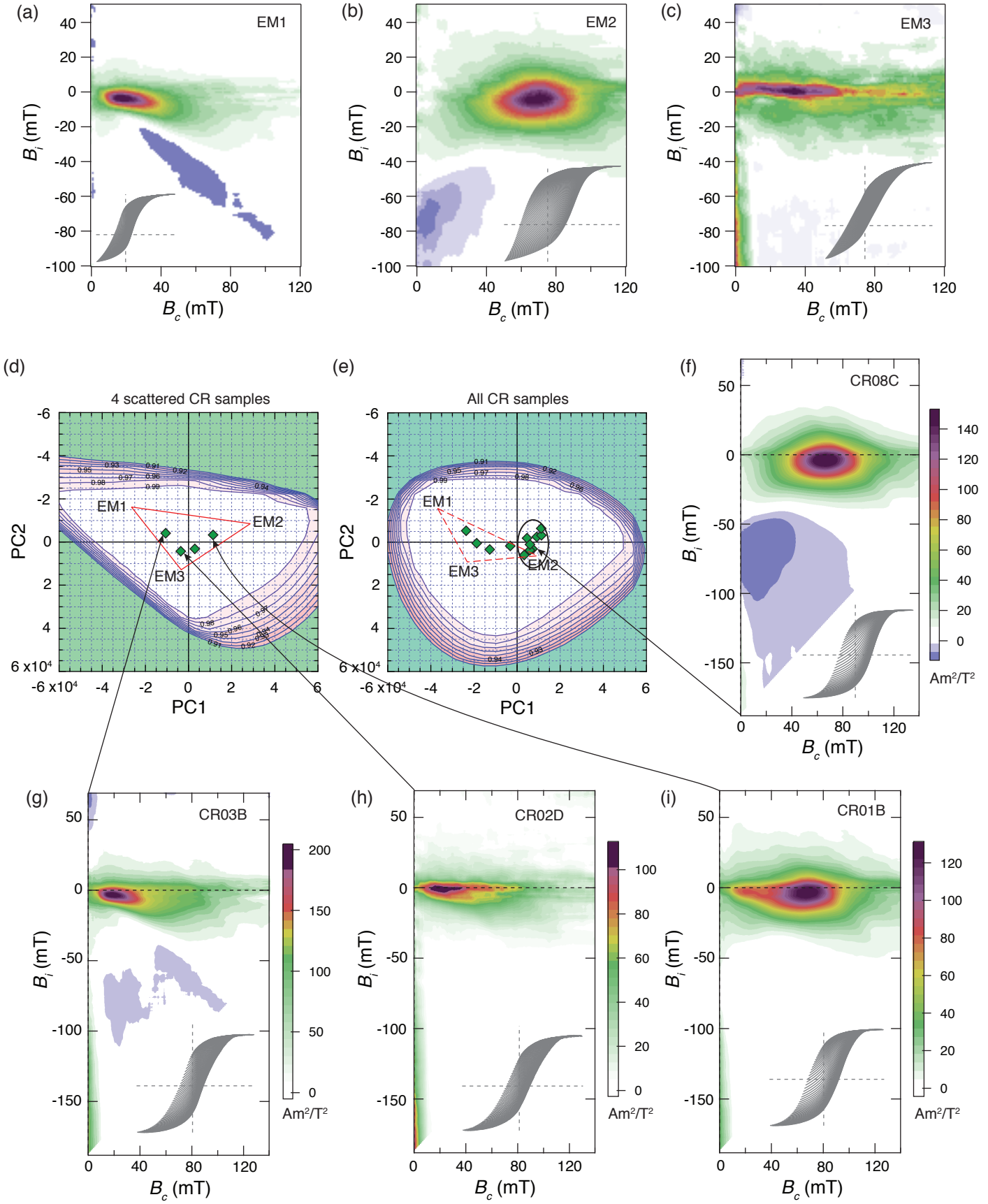
(a)
EM1
(b)
EM2
(c)
EM3
B_i (mT)
B_c (mT)
(d)
4 scattered CR samples
(e)
All CR samples
PC1
PC2
(f)
CR08C
Am²/T²
(g)
CR03B
(h)
CR02D
(i)
CR01B

Figure 7.

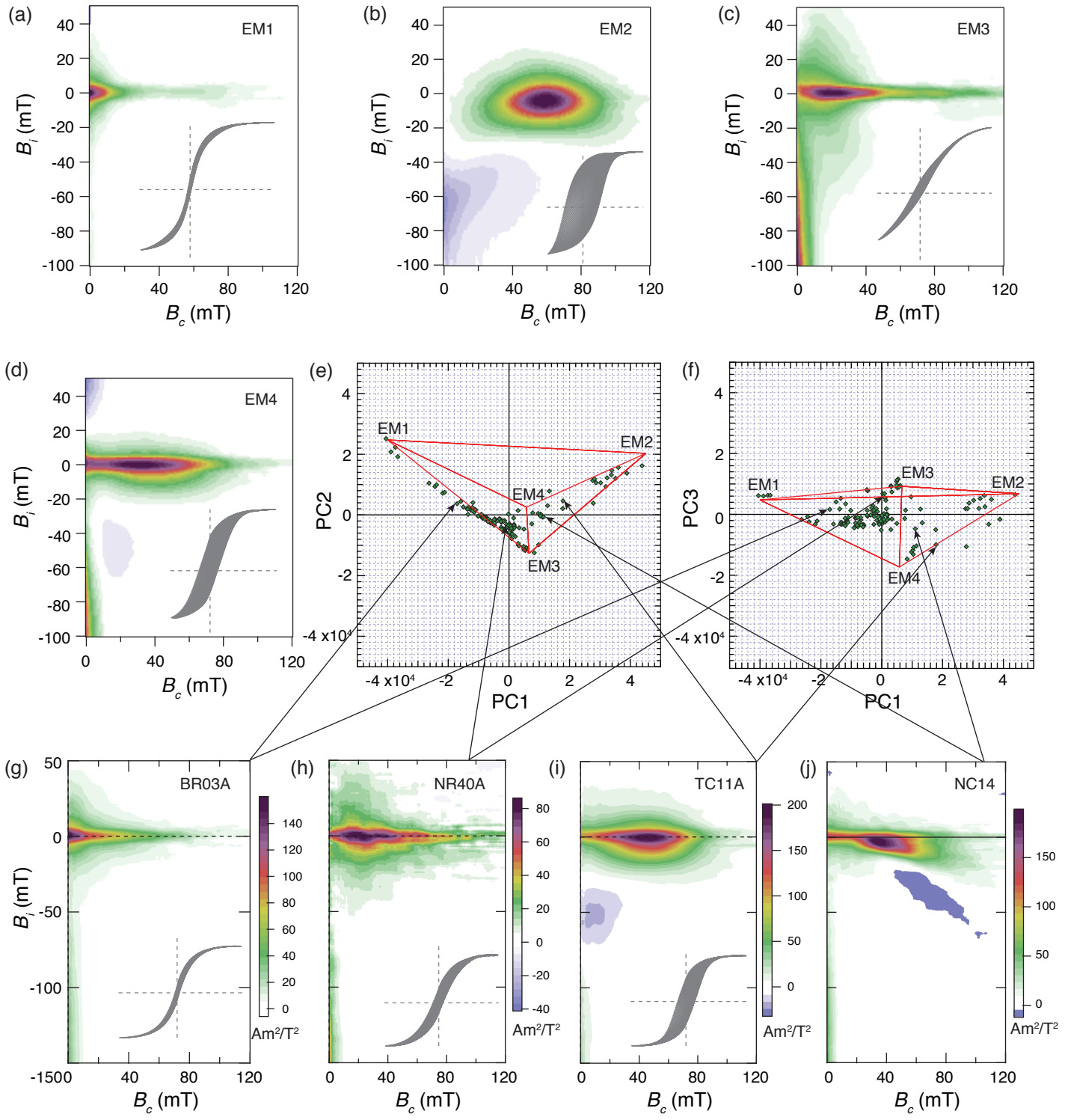
(a)
EM1
(b)
EM2
(c)
EM3
(d)
EM4
(e)
EM1
EM2
EM4
EM3
PC2
PC1
(f)
EM1
EM3
EM2
EM4
PC3
PC1
(g)
BR03A
(h)
NR40A
(i)
TC11A
(j)
NC14
B_i (mT)
B_c (mT)
Am²/T²
-4 x10⁴

Figure 8.

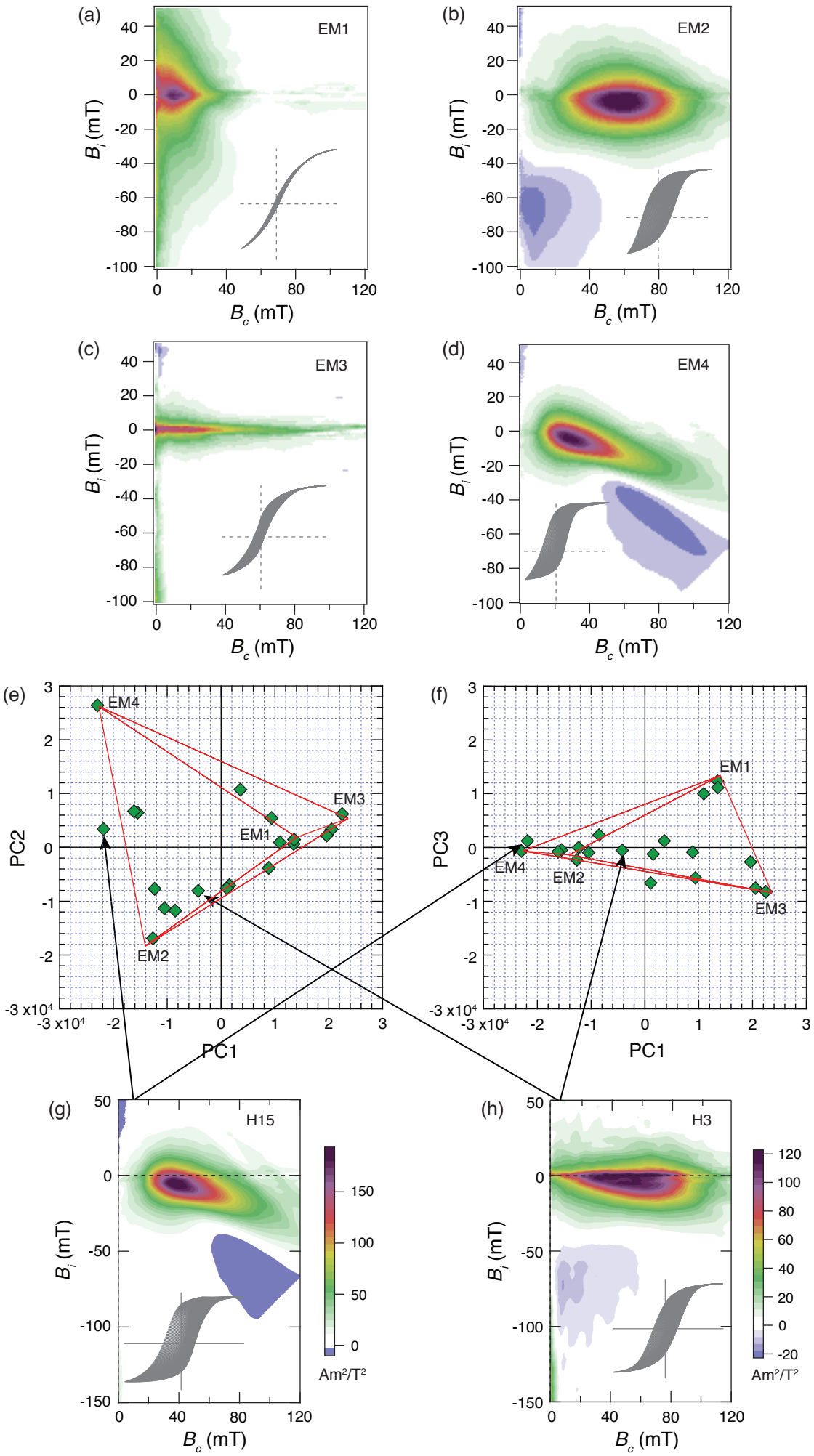
(a)
EM1
(b)
EM2
(c)
EM3
(d)
EM4
B_i (mT)
B_c (mT)
(e)
EM4
EM3
EM1
EM2
PC2
PC1
(f)
EM1
EM4
EM2
EM3
PC3
PC1
(g)
H15
(h)
H3
Am²/T²

Figure 9.

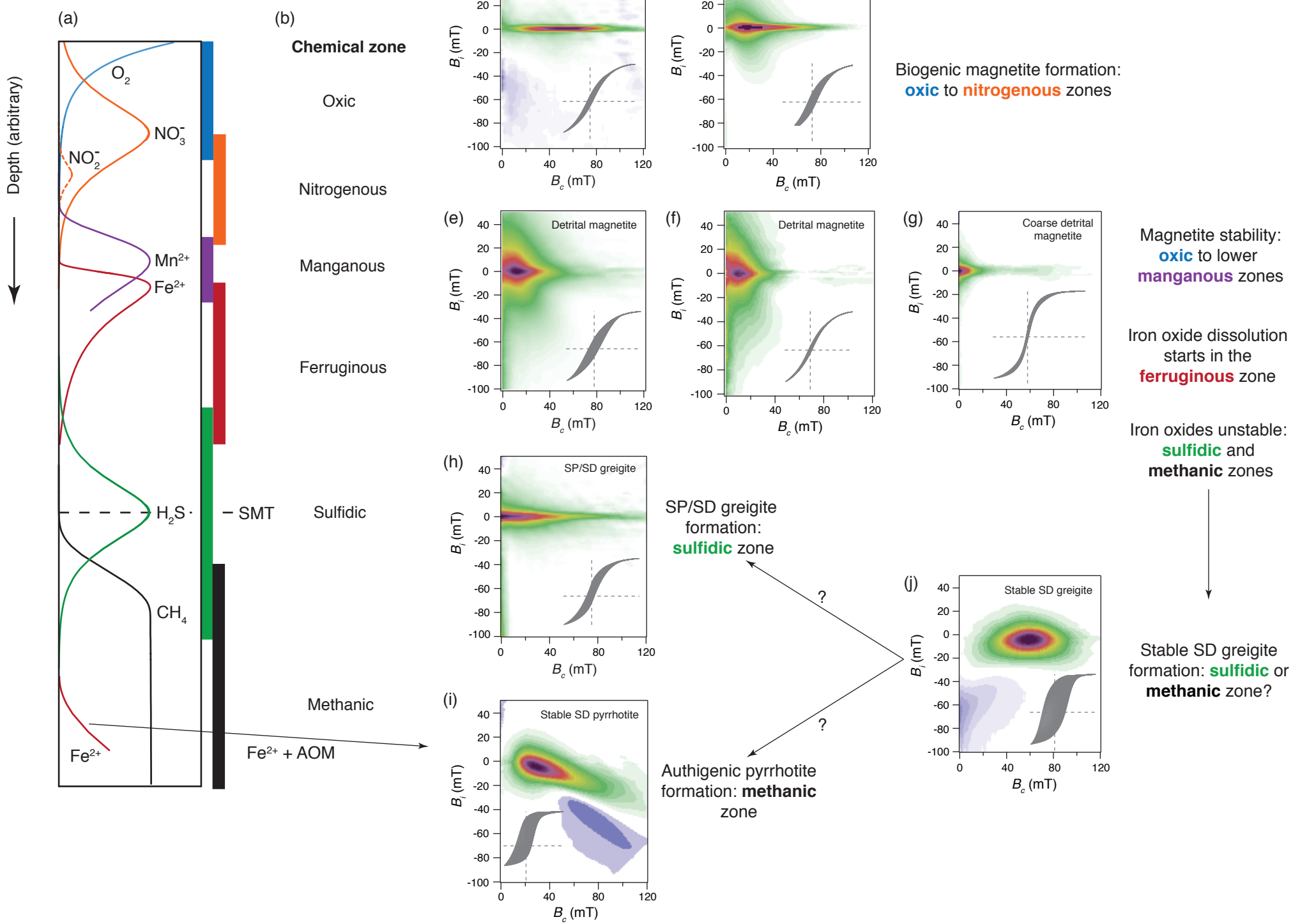
(a)
(b)
Chemical zone
Depth (arbitrary)
O_2
NO_3^-
NO_2^-
Mn^{2+}
Fe^{2+}
H_2S
SMT
CH_4
Fe^{2+}
Oxic
Nitrogenous
Manganous
Ferruginous
Sulfidic
Methanic
Fe^{2+} + AOM
(c)
Biogenic magnetite
(d)
Biogenic/detrital magnetite
Biogenic magnetite formation: oxic to nitrogenous zones
(e)
Detrital magnetite
(f)
Detrital magnetite
(g)
Coarse detrital magnetite
Magnetite stability: oxic to lower manganous zones
Iron oxide dissolution starts in the ferruginous zone
Iron oxides unstable: sulfidic and methanic zones
(h)
SP/SD greigite
SP/SD greigite formation: sulfidic zone
?
?
(i)
Stable SD pyrrhotite
Authigenic pyrrhotite formation: methanic zone
(j)
Stable SD greigite
Stable SD greigite formation: sulfidic or methanic zone?
B_i (mT)
B_c (mT)